Filling the gaps between tide gauges: Demonstrating high-resolution seasonal high tide flooding predictions using NOAA's Coastal Ocean Reanalysis

Matthew P. Conlin[1,2,*], Gregory Dusek[1], John Racliff[1,2], John A. Callahan[1,2], Karen E. Kavanaugh[1], William Brooks[1], Blake Waring[1,3], Analise Keeney[1], William Sweet[1], and Matthew J. Widlansky[4,5]

[1] National Ocean Service, National Oceanic and Atmospheric Administration (NOAA), Silver Spring, Maryland, United States of America
[2] Ocean Associates, Inc., Arlington, Virginia, United States of America
[3] Consolidated Safety Services, Inc., Fairfax, Virginia, United States of America
[4] Cooperative Institute for Marine and Atmospheric Research, School of Ocean and Earth Science and Technology, University of Hawai'i at Mānoa, Honolulu, Hawai'i, United States of America
[5] Department of Oceanography, University of Hawai'i at Mānoa, Honolulu, Hawai'i, United States of America

[*] Corresponding author
E-mail: matthew.conlin@noaa.gov

Abstract

High Tide Flooding (HTF) is a present and increasing hazard for coastal communities across the United States. NOAA provides HTF outlooks at U.S. tide gauges, however, many coastal communities lie relatively far from a tide gauge and therefore currently lack localized HTF guidance. In this study, we demonstrate an approach to generate spatially-continuous daily predictions of HTF at 400-500 m resolution out to a year into the future, by combining NOAA's monthly HTF outlook framework with the newly-released Coastal Ocean Reanalysis (CORA). Using CORA to derive daily HTF predictions at tide gauges, as compared to using gauge observations, results in average HTF model skill reduction of ≤5% using three different statistical metrics at one month lead time. Further, stations which obtain statistically skillful HTF predictions using gauge data also do so using CORA for 94% of cases. The results suggest that CORA could enable skillful HTF predictions away from tide gauges, supporting the possibility of providing high resolution HTF outlooks for much of the U.S. coastline. The potential value of these spatially continuous HTF predictions is illustrated by identifying communities near Charleston S.C. with different CORA-derived local HTF risk than that provided by the closest tide gauge. Finally, we describe outstanding questions and needs for the scaling of these results to an operational national-scale monthly HTF outlook.

1. Introduction

High tide flooding (HTF), i.e. typically minor coastal flooding that can occur without a storm (e.g. Sweet et al., 2022), is a present and increasing hazard for coastal communities across the United States. The height between impact-inducing flood levels and typical high tides continues to become smaller in many regions around the country experiencing relative sea level rise (SLR; Sweet et al., 2022). Numerous studies have indicated that HTF already occurs regularly today (Goodman et al. 2018; Fant et al., 2021; Sweet et al., 2021; Li et al., 2022; Sun et al., 2023) and will increase in frequency and severity with continued SLR in the coming decades (e.g. Vandenberg-Rodes et al., 2016; Dahl et al., 2017; Burgos et al., 2018; Thompson et al., 2021; Sweet et al., 2022). Though immediate damage is not as impactful as major flooding due to coastal storms, the cost of recurrent HTF may be greater due to cumulative impacts to coastal infrastructure and economies. These impacts can include damage to transit infrastructure, reduced visits to impacted storefronts, damage to private property contributing to decreased real estate values, and degradation of wastewater treatment facilities (Obeysekera et al., 2011; Moftakhari et al., 2017; Hummel et al., 2018; Jacobs et al., 2018; McAlpine & Porter, 2018; Hino et al., 2019; May et al., 2023).

In response to the threat of HTF, NOAA produces HTF outlooks at many tide gauges in the U.S. These span timeframes from annual outlooks supplemented by decadal projections that aid in budgeting and long-term planning (NOAA, n.d.); to monthly outlooks that provide daily HTF probabilities from the present out to one-year to facilitate preparedness (NOAA, 2025). While the HTF outlooks are a critical advancement for preparedness and mitigation of HTF impacts, they are applied only to tide gauge observations from the National Water Level Observation Network (NWLON; Miller & Luscher, 2019). NWLON sites are sparse and many coastal communities are far from a gauge. Further, due to small scale variability driven by local bathymetry/topography, riverine inputs, and other processes, water levels and flood thresholds

at a NWLON site are not necessarily representative of locations even a short distance away (e.g. Thompson et al., 2016; Parker & Ollier, 2017).

To address these spatial gaps in data availability and flood guidance, NOAA initiated the Coastal Ocean Reanalysis (CORA), which provides 44 years of hourly water levels at 400-500 m resolution along the entirety of the U.S. Gulf and East Coasts (GEC) as well as the Caribbean (Rose et al., 2024; Keeney et al., 2025). The advent of CORA could make it possible to expand the HTF outlooks between and away from NWLON stations, which would enable unprecedented local HTF guidance across the U.S. These spatially continuous HTF outlook products would provide coastal communities far from NWLON stations with new, historical, and local information to aid in planning and flood mitigation efforts.

In this study, we demonstrate an approach to generate a spatially continuous monthly HTF outlook between tide gauges by leveraging CORA. We first compared CORA-derived HTF predictions with those from tide gauge observations at NWLON stations in the GEC to quantitatively assess the skill of CORA-derived HTF predictions at the stations. We then derived HTF predictions at shoreline-following sets of CORA nodes near Charleston, S.C. to demonstrate that spatially-continuous HTF predictions between NWLON stations can provide valuable localized HTF guidance.

2. Background

2.1. The seasonal HTF model and monthly HTF outlook

The seasonal HTF model (HTF model hereafter) was introduced by Dusek et al. (2022) and serves as the basis for NOAA's monthly HTF outlook, which is provided at many NWLON stations (Kavanaugh et al., 2023; NOAA CO-OPS, 2024; NOAA, 2025). The HTF model combines tide predictions with climatologies of hourly non-tidal residuals (NTR; the difference

between observed water levels and tide predictions), long-term linear trends of relative sea levels, and the damped persistence of monthly mean sea level (MSL) anomalies to provide daily predictions of HTF probability out to one year in the future. The NTR climatologies are developed by binning 23 years of hourly water levels by calendar month and tide decile and then adjusting for the linear long-term trend in MSL. The predicted NTR for any hourly timestep is given as a probability distribution that is assumed to be Gaussian with a mean of:

$$\mu_{clim}(t) = \mu_{month}(t) + \mu_{tide}(z) + p(t), \quad (1)$$

where $\mu_{month}(t)$ is the mean NTR for the calendar month in which time t lies, $\mu_{tide}(z)$ is the mean NTR for the tide level decile in which predicted tide z lies relative to the total mean NTR (termed the tide level adjustment factor in Dusek et al. [2022]), and $p(t)$ is the damped persistence value of the MSL anomaly to use for time t. Calculation of the standard deviation of the Gaussian σ_{NTR} follows a similar convention. The predicted NTR distribution is then combined with the tide predictions and SLR trend and compared to an input flood threshold to determine the probability of flooding as the area under the model-predicted water level distribution that is above the flood threshold. Daily cumulative flood probabilities P_{day} are then computed from the 24 corresponding hourly values $P(t)$ as the maximum hourly value that day P_{max} plus the portion of each remaining value that day that is independent of the autocorrelation of the NTR signal $r(t)$:

$$P_{day} = P_{max} + \sum_{t=1}^{23} \left[P(t)\big(1 - r(t)\big)\right]. \quad (2)$$

Dusek et al. (2022) applied the HTF model to 98 NWLON gauges in the U.S. Without considering the persistence of the MSL signal ($p(t) = 0$, which they termed the “climatological

model"), the HTF model was found to skillfully predict HTF days at 61 of the 92 gauges that experienced at least 10 HTF days using a Brier Skill Score (BSS) for a retrospective assessment. The performance of the HTF model was found to scale with tidal contribution to the total variance in the water level signal. This is because, while some information about temporal patterns of weather events can be retained in the NTR climatologies, flooding driven by individual weather events cannot be predicted by the model. Hence, model performance is weaker in locations like the Gulf, where the tidal signal is small compared to the contribution of weather events to flooding. Similarly, model performance was found to scale with the distance between the flood threshold and mean water level, as tidal contributions to flooding become increasingly important as the average daily high tide approaches the flood threshold. Inclusion of the MSL persistence (termed the "persistence model"), as used in this work, improved model performance primarily in the Pacific Islands and southern West coast.

2.2. The Coastal Ocean Reanalysis (CORA)

The NWLON is the authoritative source for water level data in the U.S. and supports such crucial applications as maritime economic boundary delineation and safe and efficient marine navigation (Sweet et al., 2018; Miller & Luscher, 2019; Dusek et al., 2024). Large stretches of U.S. coastline, however, are relatively far from an NWLON station; in some cases hundreds of kilometers separate tide gauges. Therefore, many coastal communities do not have adequately representative NWLON water level observations. CORA was developed to fill these data gaps and provide more localized information about water levels, waves, and flooding (see Keeney et al, 2025).

CORA provides hourly water level data from 1979 through 2022 over an unstructured mesh that contains 1.8 million points for the Gulf and Northwestern Atlantic domain at typically 400-500 m resolution along the coast (Rose et al., 2024; Keeney et al., 2025; Fig. 1). Detailed

model setup and information is provided in Keeney et al. (2025) and will be summarized below. CORA is created using the two-dimensional barotropic ocean circulation model ADCIRC coupled with the spectral wave model SWAN. The open offshore boundary of the northwestern Atlantic model domain extends in an arc from Novia Scotia to Suriname, reaching eastward to the 55° W meridian. The model is forced with atmospheric pressure and 10 m wind velocities extracted from the ERA5 atmospheric reanalysis (Hersbach et al., 2020) as well as astronomical tides at the offshore boundary in the form of 10 principal tidal constituents extracted from TPXO (Egbert & Erofeeva, 2002). Water level observations from 53 NWLON stations distributed throughout the GEC are low pass filtered at a 4-day cutoff period and dynamically assimilated into the model to capture non-barotropic sea level trends and variability. CORA therefore represents a reanalysis of local relative sea levels driven by both eustatic sea level changes and spatially variable rates of vertical land motion. Observations from 59 other NWLON stations in the GEC are used for model validation (Keeney et al., 2025). Importantly, only open-coast stations are used in the data assimilation (Keeney et al., 2025), meaning that validation (unassimilated) stations are in non-open coast (riverine, estuarine, and bay) environments.

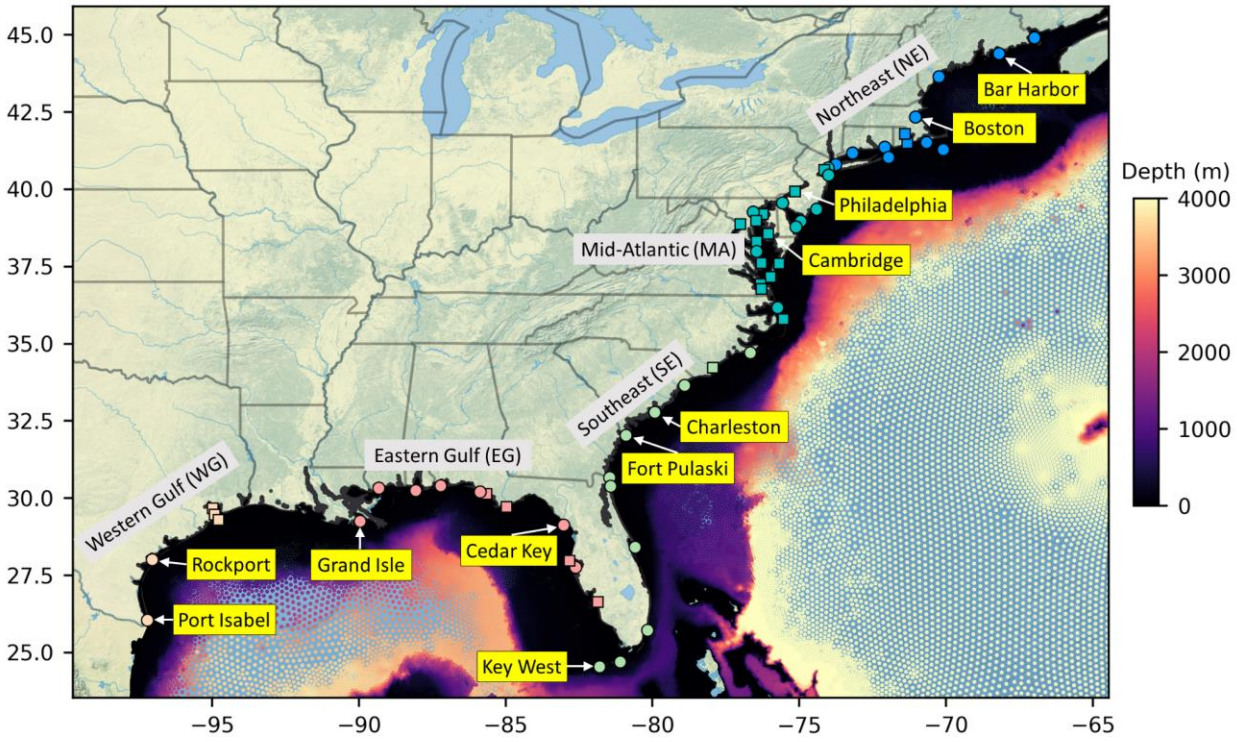

Fig. 1. Overview of the spatial domain of CORA and NWLON stations considered in this work. Stations shown in later figures and/or specifically called out in the text are labelled. Stations depicted as circles (squares) are (are not) assimilated in CORA. The colors of the stations in each labelled region correspond to those used in later plots. Map source: Natural Earth.

Rose et al. (2024) validated water levels from a preliminary version of CORA (version 0.9) compared to NWLON gauge observations. They assessed performance for GEC stations over the period 1979-2021, and found that long term linear trends, annual variability, monthly variability, and hourly nontidal residual variability from CORA water levels compared closely to observations. For example, the average linear trend from CORA between 1993 and 2020 was only 7% less than that from the gauges, while average monthly water level standard deviation from CORA was only 8% less than that from the gauges. Performance was generally stronger for the East Coast than the Gulf Coast, and weakest at stations far up rivers, as riverine processes are not included in the model. The transfer of spatially-varying CORA errors to CORA-derived HTF predictions is explored further in Section 5.

Here, we used a newer version of CORA (1.1) compared to what Rose et al. (2024) assessed. The primary difference between the two versions (0.9 and 1.1) involves the data assimilation scheme, with improved performance in a few areas such as the Gulf Coast (Keeney et al., 2025). Keeney et al. (2025) assessed the overall performance of CORA version 1.1 water levels relative to NWLON stations and found a RMSE of 0.15 m at validation (non-assimilated) stations and 0.11 m at assimilated stations.

3. Methods

To understand the accuracy of CORA-derived HTF predictions, we first assessed differences between CORA-derived and gauge-derived HTF predictions at NWLON stations in the GEC. We then applied the HTF model to two subsets of shoreline-following CORA nodes around Charleston S.C. to demonstrate the potential value of high spatial resolution HTF predictions enabled by CORA.

3.1. HTF model setup

Following Dusek et al. (2022), the HTF model was fit using 23 years of hourly water level observations and HTF predictions were completed at varying lead times. For example, the model was fit using hourly observations (from tide gauges and CORA nodes) from January 1, 1997 through December 31, 2019 (as in Dusek et al., 2022), and then hourly HTF predictions were made for January 2020 (one month lead time), February 2020 (two month lead time), March 2020 (three month lead time), etc. The training period was then slid forward one month and the process repeated, such that February 2020 was predicted at 1 month lead time, etc. HTF predictions were made and evaluated for 2020 through 2022, representing the three most recent years currently available in CORA (note that Dusek et al., 2022 used a retrospective skill assessment over the training period). Three years were chosen as the evaluation period as a balance between capturing a relatively large number of flooding events and computational

resources. In the comparison between gauge-derived and CORA-derived HTF predictions, we consider results at one month lead time only, though results at three month lead time, for example, were very similar (S1 Appendix).

3.2. Preparation CORA data

CORA water levels were obtained from the NOAA Open Data Dissemination platform (NOAA NOS CO-OPS, n.d.). Publicly available Python code notebooks were used to facilitate data access (NOAA CO-OPS, 2025). To compare with tide gauges, CORA water levels at the locations of the NWLON stations were derived using an inverse distance-weighted interpolation to the nodes comprising the mesh element encompassing the station, similar to Rose et al. (2024). We considered 61 stations in total. The CORA timeseries always indicated “wet” conditions (no missing data) at 58 of these 61 considered stations; at the remaining three stations- Apalachicola, F.L.; Bay Waveland Yacht Club, M.S.; and Port Isabel, T.X.- CORA data were dry <0.1% of the training period. We considered the same NWLON stations as Dusek et al. (2022) except that we added two stations that were not used (Eastport, M.E. and Money Point, V.A.) and did not consider three stations with incomplete data records during the evaluation period (2020 through 2022; Naples, F.L., Sabine Pass, T.X., and Corpus Christi, T.X.). S2 Table provides details on these and all possible GEC NWLON stations. Of the 61 considered stations, more were assimilated in CORA (38) than were not (23). Assimilated stations are in open-coast environments, while non-assimilated stations are not.

For the Charleston, S.C. case study, CORA data from subsets of nodes following the coast were extracted and run through the HTF model as described in Section 3.1. The shoreline-following nodes were derived in different ways for the two spatial scales considered. Between the neighboring Fort Pulaski, G.A. and Charleston, S.C. NWLON stations, a vector layer was created of points 500 m from the shoreline- defined using NOAA’s Continuously

Updated Shoreline Product (NOAA NGS, 2025)- spaced at 1 km in the alongshore. After some manual refinement to ensure smoothness and that only CORA nodes that were nearly always inundated were included, CORA data were interpolated to these points using an inverse distance-weighted interpolation. Within Charleston Harbor and the immediate vicinity, a shoreline was defined at the interface between nodes that always remain wet and those that do not. This interface was developed using an output file from each ADCIRC model year delineating nodes that were always inundated, and further refining to those that were on a mesh element which also contained a node that was not always inundated.

3.3. Computation of physical quantities from CORA

In addition to water level observations, the HTF model relies on other physical quantities: datums, flood thresholds, SLR trends, and tide predictions. In general, standard methods are utilized through existing products to provide each of these quantities at NWLON stations (e.g. Parker, 2007; Zervas et al., 2009; Dusek et al., 2022). However, these quantities must be computed at CORA nodes to provide input to the HTF model. Our approach is detailed below.

3.3.1. Datums and flood thresholds

Many NWLON stations have established impact-based flood thresholds set by local National Weather Service Weather Forecast Offices, and multiple methods use these established flood thresholds to estimate impact-based flood thresholds anywhere (e.g. Sweet et al., 2018; Mahmoudi et al., 2024; Piecuch et al., 2025). Impact-based flood thresholds at NWLON stations in the GEC are typically between 0.5 and 0.6 m above mean higher high water (MHHW) using the method described in Sweet et al. (2018). Since no single threshold describes all types of localized impacts, here we considered HTF predictions over multiple flood thresholds taken at 15 cm (~0.5 ft) increments from 0.15-0.60 m (0.5-2 ft) above MHHW. This approach aims to facilitate mapping of inundation impacts over a range of water levels and elicit

a better sense of CORA-derived HTF prediction performance across multiple possible flood thresholds.

While flood thresholds are relative to MHHW, CORA is referenced to the MSL datum. To relate CORA observations to MHHW, datums were computed at each CORA node from the CORA hourly water level timeseries using the First Reduction method in the Tidal Analysis Datums Calculator (TADC; Lictate et al., 2017). The TADC identifies high and low waters from a low-pass filtered (at four cycles per day) water level signal and uses these to compute the standard tidal datums (MSL, MHHW, etc.). The computation was performed over the same 19-year National Tidal Datum Epoch used at NWLON stations (1983-2001). CORA water levels were placed onto the derived MHHW datum by setting this value as the zero-level of the timeseries.

3.3.2. Tide predictions

Tide predictions serve as the core of the HTF model, as they provide a deterministic water level into the future that serves as the baseline atop which derived NTR climatologies and SLR trends are applied. At NWLON stations with data records longer than 19-years (all stations considered here), tide predictions are computed using harmonic analysis of hourly observations using at least 5 years for high-frequency harmonics and 19 years for low-frequency harmonics for a standard set of 37 harmonic constituents that contribute the majority of the tidal signal (Parker, 2007). For CORA data, the Unified Tidal Analysis (UTide) software package (Codiga, 2011) was used to perform the harmonic analysis and compute tidal constituents and tide predictions. Tidal constituents were computed from the hourly detrended CORA dataset using the 19 year period 2002-2020 with nodal corrections applied and with UTide able to determine the constituents to include based on a built-in signal to noise ratio analysis. Derived constituents

were then used to reconstruct tide predictions over any period relative to MHHW (see section 3.3.1).

3.3.3. Long-term relative sea level trends

To adjust the (trendless) tide predictions for the observed SLR trend, Dusek et al. (2022) calculated a linear trend from 1980 through 2019 at each NWLON site following Zervas (2009). This method computes the trend using a lag 1 autoregressive linear model of monthly mean sea level (MSL) with the mean annual cycle removed. We used the same technique and time period to compute the long-term trend for each CORA node.

3.4. Quantification of HTF model performance

Multiple metrics were used to quantitatively assess differences between CORA-derived and gauge-derived HTF predictions at NWLON stations. To assess the relative change in HTF predictions, we binned the HTF probabilities into hazard levels (HLs). The monthly HTF outlook discretizes HTF probabilities into three “likelihood” categories: unlikely for <5% probability, possible for 5-50% probability, and likely for ≥ 50% probability (NOAA, 2025). Here, we chose to use the HLs employed by the NOAA Climate Prediction Center’s Probabilistic Hazard Outlooks (NWS CPC, 2025): low risk of HTF for 0-20% probability, slight risk of HTF for 20-40% probability, moderate HTF risk for 40-60% probability, and high risk of HTF for 60-100% probability (all levels except the last are lower bound inclusive and upper bound exclusive). Using these HLs, we defined “HL agreement” as the percentage of daily CORA-derived HTF predictions that achieved the same HL as gauge-derived HTF predictions. Further, based on enumerating the HLs (e.g. 1=low risk, 2=slight risk, 3=moderate risk, 4=high risk), we also assessed the bias (mean error) and mean absolute error (MAE) of daily CORA-derived HTF predictions relative to gauge-derived HTF predictions. For example, a HL MAE of 0.1 indicates an average absolute HL error of 10% of a hazard level. These metrics provide practical

guidance on the extent to which CORA-derived HTF predictions could yield the same decision-support information as gauge-derived HTF predictions.

Additionally, we utilized the continuous ranked probability score (CRPS; Wilks et al., 2011) to evaluate the performance of the model in terms of predicted water levels. The CRPS is effectively the squared area between the HTF model-derived water level Gaussian cumulative distribution function (CDF) and the step function representing the observed water level:

$$CRPS = \int_{-\infty}^{\infty} [F_f(\eta) - H(\eta - \eta_0)]^2 \delta\eta, \quad (3)$$

where F_f is the model-derived CDF, H is the Heaviside step function, and η_0 is the observed water level. The CRPS can be interpreted as the average model performance integrated across all possible HTF thresholds. We computed and compared the average CRPS of daily maximum water levels for the 2020 through 2022 prediction period for both gauge-derived and CORA-derived predictions.

Following Dusek et al. (2022), we also evaluated the performance of the HTF model- for both CORA and gauge input- in terms of predicted flood days. We identified the stations where the Brier Skill Score (BSS) is greater than the standard error of the BSS (BSS_{SE}), as computed following Bradley et al. (2008). The BSS was computed as:

$$BSS = 1 - \frac{BS}{BS_{clim}}, \quad (4)$$

where BS is the Brier Score of the model predictions and BS_{clim} is the BS of HTF predictions made using the climatological mean observed probability at all timesteps (Wilks et al., 2011). BS was computed as:

$$BS = \frac{1}{n}\sum_{t=1}^{n} \quad (P(t) - o(t))^2 \,, \tag{5}$$

where n is the timeseries length, t is the timestep, P is the model-derived HTF probability, and o is the observed flood value ($o(t) = 1$ if HTF occurred, $o(t) = 0$ if HTF did not occur; Wilks et al., 2011). The stations for which $BSS > BSS_{SE}$, which are termed "skillful", were compared for CORA-derived and gauge-derived predictions. Additionally, to provide a more concise comparison, we computed the BSS of CORA-derived HTF predictions using the gauge-derived HTF predictions as the reference model, which we term the relative Brier Skill Score ($rBSS$):

$$rBSS = 1 - \frac{BS_{CORA}}{BS_{gauge}}. \tag{6}$$

The $rBSS$ can be interpreted as a proportional performance change, according to the BS metric, when using CORA as input vs. using gauge data as input to the HTF model. $rBSS < 0$ indicates weaker model performance using CORA ($BS_{CORA} > BS_{gauge}$), while $rBSS > 0$ indicates stronger model performance using CORA ($BS_{CORA} < BS_{gauge}$).

Finally, we also computed Relative/Receiver Operating Characteristic (ROC) curves for gauge-derived and CORA-derived HTF predictions (e.g. Mason & Graham, 1999; 2002). ROC curves plot the true positive rate as a function of the false positive rate of HTF occurrence for all possible HTF probability warning levels (the model-derived HTF probability at or above which HTF is deemed to occur). For each flood threshold, an average curve was computed for each spatial region (see Fig. 1) using both gauge and CORA input. We also computed the area under these curves (AUC; Mason & Graham, 2002) as measures of model performance and quantified the decrease in AUC for CORA-derived HTF predictions relative to gauge-derived HTF predictions. $AUC = 1$ indicates perfect model performance, while a random guess obtains $AUC = 0.5$.

4. Results

4.1. CORA datums, tide predictions, and SLR trends

CORA and gauge MHHW datums were highly correlated ($r = 0.99$) with a root mean squared error (RMSE) of 8 cm and slight overall negative bias of 4 cm (Fig. 2a). For the period 1997 through 2022, the RMSE of hourly CORA-derived tide predictions relative to the published values at the NWLON stations was 18 cm, though was 11 cm for tides above MHHW (those responsible for HTF; Fig. 2b). CORA trends were relatively less correlated with the gauges ($r = 0.65$). The RMSE of CORA-derived trends relative to the published values at the NWLON stations was 1.27 mm/yr (Fig. 2c), however not considering Eagle Point, TX the RMSE was 0.74 mm/yr. Eagle Point, TX has been strongly impacted by land subsidence due to oil and gas extraction (Qiao et al., 2023), processes CORA does not capture at this unassimilated station (Fig. 2c).

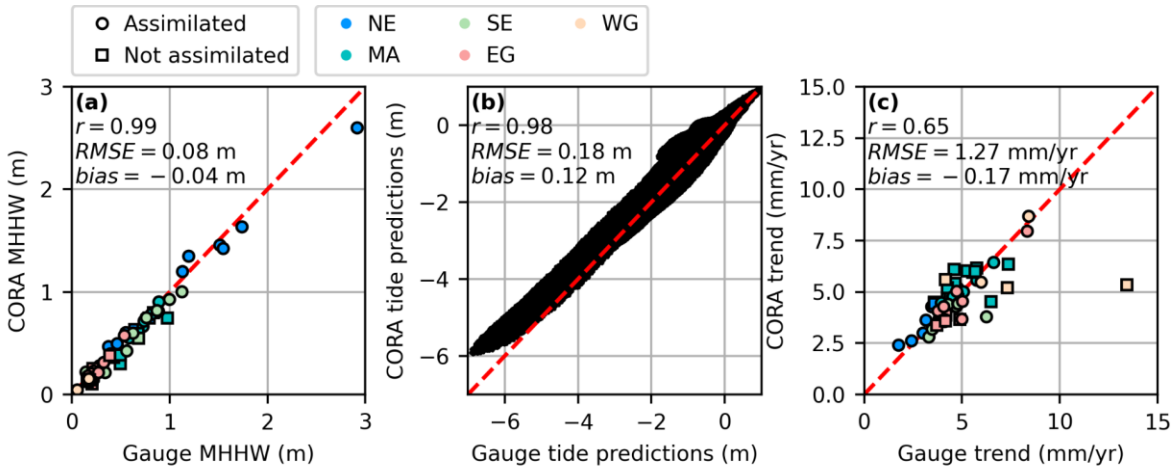

Fig. 2. Comparison of CORA-derived physical quantities with those published at the NWLON stations used in this work. (a) MHHW elevation relative to MSL, (b) Tide predictions relative to MHHW, and (c) linear relative sea level trend.

4.2. Accuracy of CORA-derived HTF predictions

In general, CORA produced similar HTF predictions to the gauges at the NWLON stations, and in particular captured the same peak events. For example, Fig. 3 shows example timeseries of daily HTF probability above $MHHW + 0.30$ m over the prediction period at one-month lead for selected stations, where the agreement between gauge-derived and CORA-derived HTF predictions is qualitatively clear. There were, however, cases of underprediction, particularly for some of the highest-probability peaks derived from the gauge at Port Isabel, TX (Fig. 3f). Cases of overprediction were also apparent, and can be seen at all example stations in Fig. 3.

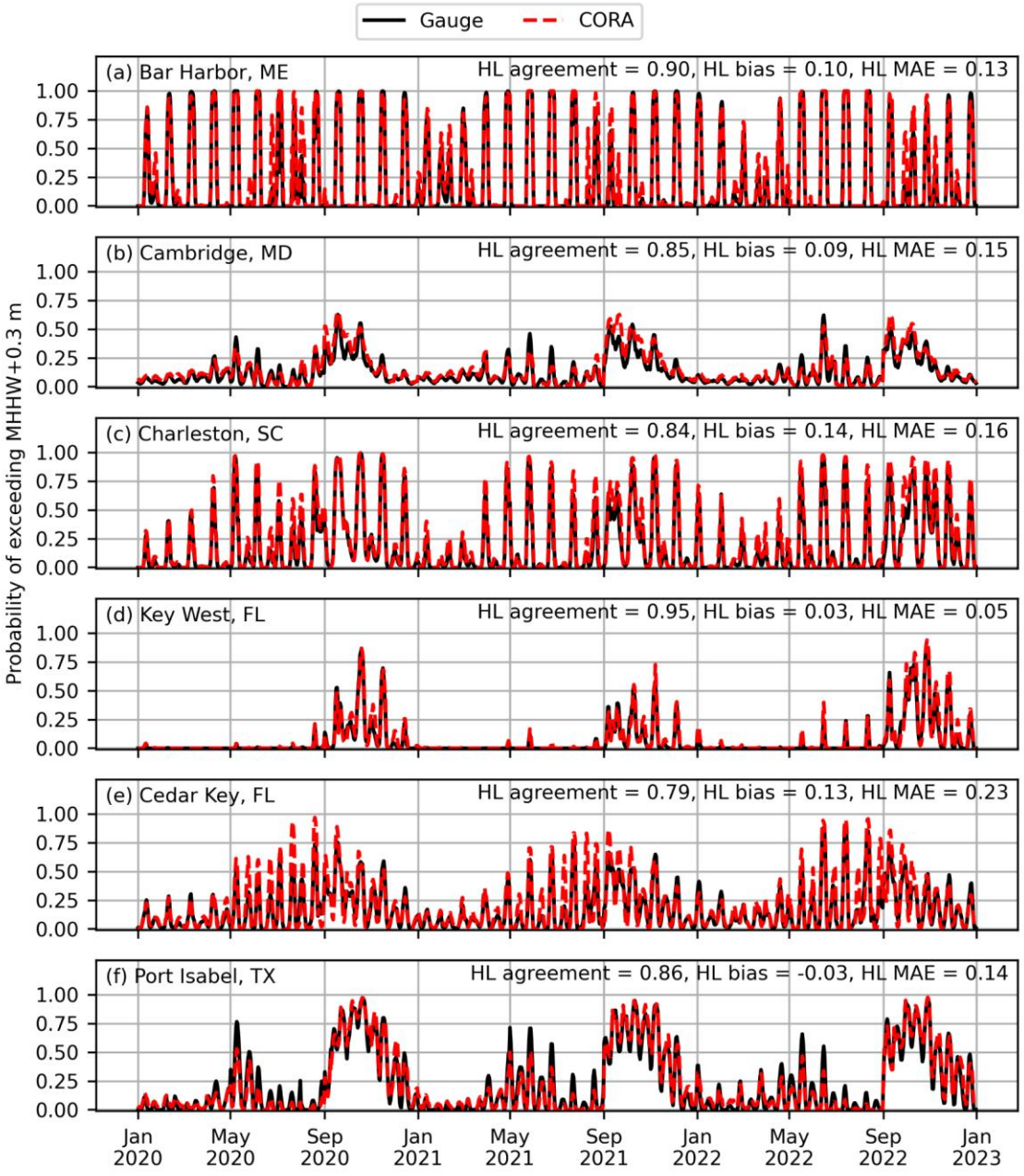

Fig. 3. Selected examples of gauge-derived (black) and CORA-derived (red) daily high tide flooding probabilities at one-month lead above $MHHW + 0.30$ m. At least one station from each of the five geographic regions (see Fig. 1) is shown. Hazard level statistics for each station are also shown.

Quantitatively, CORA produced the same HL as the gauges the majority of the time, as shown in Fig. 4 and Table 1 and for all stations individually in S3 Table. For flood thresholds $\geq MHHW + 0.45$ m, HL agreement was $\geq 84\%$ on average within each region (Fig. 4a, Table 1),

while average absolute HL biases were ≤ 0.09 (Fig. 4b, Table 1). HL agreement (Fig. 4a), bias (Fig. 4b), and MAE (Fig. 4c) were inversely related to flood threshold: HL agreement increased from an overall average value of 77% for a flood threshold of $MHHW + 0.15$ m to 99% for a flood threshold of $MHHW + 0.60$ m, while bias decreased from 0.08 to 0.00 and MAE decreased from 0.26 to 0.01 (Table 1). HL biases tended to be slightly positive (CORA yielding increased HL relative to the gauge) on average across flood thresholds by <0.08, except the WG where the average bias across flood thresholds was negative at -0.09 (Table 1). Note that all values given above and below exclude Grand Isle, LA and Rockport, TX, where errors in CORA water levels and tide predictions led to strong overprediction of HTF probabilities (S4 Appendix).

Table 1. Average values of HL agreement, bias, and MAE, respectively, within each region (see Fig. 1) and for each considered flood threshold at one month lead.

Region	N[1]	$MHHW + 0.15$ m	$MHHW + 0.30$ m	$MHHW + 0.45$ m	$MHHW + 0.60$ m	**mean**
NE	12 (10,2)[1]	77% | 0.21 | 0.28	87% | 0.11 | 0.16	94% | 0.01 | 0.07	97% | -0.01 | 0.03	**89% | 0.08 | 0.14**
MA	22 (9,13)[1]	78% | 0.14 | 0.24	82% | 0.09 | 0.19	97% | 0.01 | 0.03	100% | 0.00 | 0.00	**89% | 0.06 | 0.11**
SE	11 (10,1)[1]	80% | 0.08 | 0.21	88% | 0.05 | 0.12	97% | 0.01 | 0.03	100% | 0.00 | 0.00	**91% | 0.04 | 0.09**
EG	10 (6,4)[1]	77% | 0.02 | 0.24	84% | 0.01 | 0.17	98% | 0.01 | 0.02	100% | 0.00 | 0.00	**90% | 0.01 | 0.11**
WG	4 (1,3)[1]	71% | -0.07 | 0.33	62% | -0.21 | 0.45	84% | -0.09 | 0.17	100% | 0.00 | 0.00	**79% | -0.09 | 0.24**
mean		**77% | 0.08 | 0.26**	**81% | 0.01 | 0.22**	**94% | -0.01 | 0.06**	**99% | 0.00 | 0.01**	

[1]N represents the number of NWLON stations used for the comparison, with values in parenthesis representing the number of stations that are and are not assimilated in CORA, respectively.

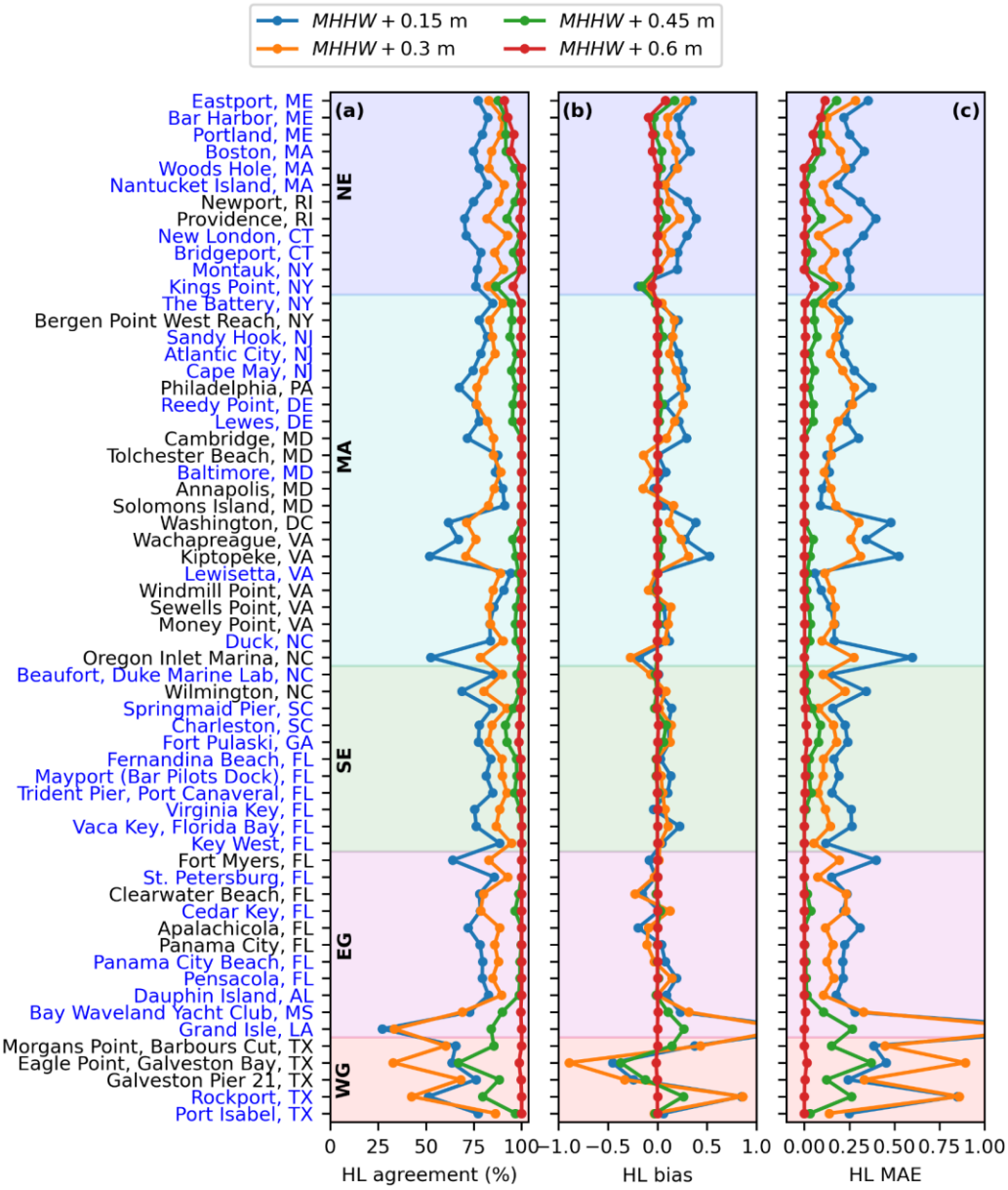

Fig. 4. Comparison of high tide flooding hazard levels (HL) derived from CORA relative to those derived from gauges for all flood thresholds considered over the period 2020 through 2022 at one month lead. (a) The percentage of daily CORA-derived high tide flooding predictions that obtain the same HL as those derived from the gauge. (b-c) The bias (b) and mean absolute error (c) in enumerated daily HL for CORA-derived high tide flooding predictions relative to those from the gauge. The geographic regions (see Fig. 1) are shown by the shading and labeled. Station names written in blue (black) are (are not) assimilated in CORA.

Using the CRPS, performance of the HTF model declined by just 5% on average when CORA input was used instead of gauge data (Fig. 5). On average, the largest performance degradation was found in the EG (8%) and the smallest was found in the MA (2%; 5-7% in the

NE, SE, and WG). At 11 of the 61 stations, primarily in the MA (5 out of 11), CORA input yielded stronger HTF model performance than gauge data. The average increase in performance at these stations was only 3%.

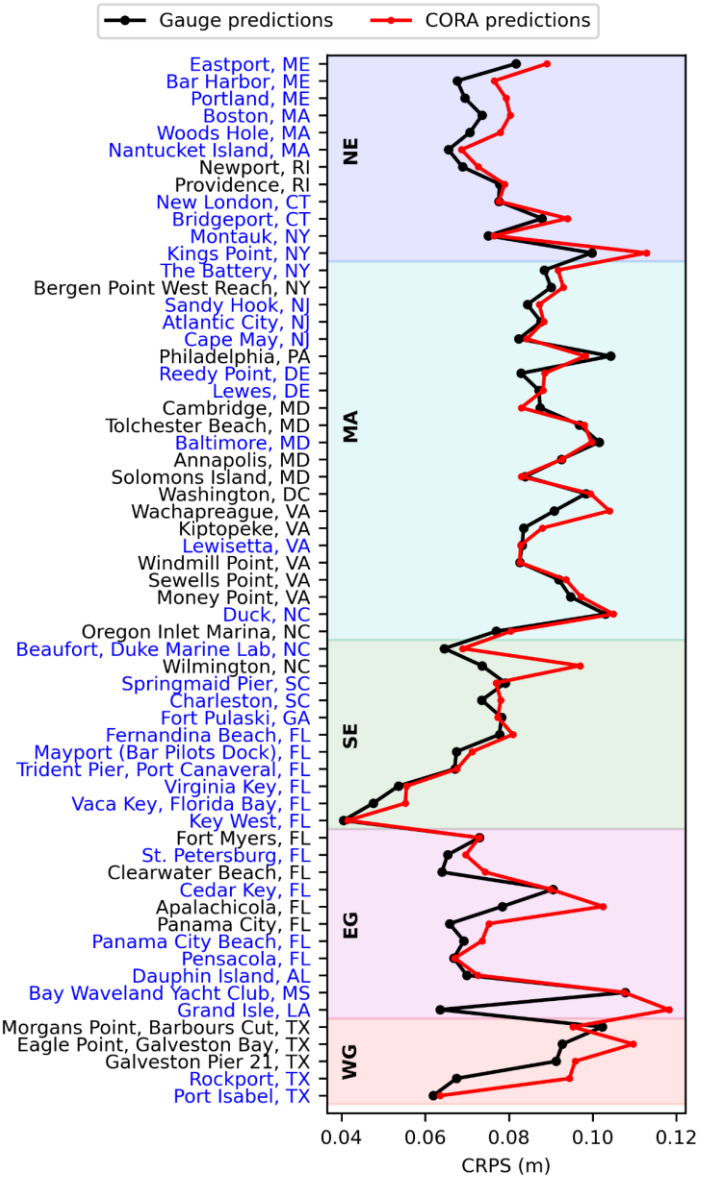

Fig. 5. Continuous Ranked Probability Score (CRPS) of daily maximum water levels over the period 2020 through 2022 at one month lead for gauge-derived (black) and CORA-derived (red) probabilistic predictions of water level. The geographic regions (see Fig. 1) are shown by the shading and labeled. Station names written in blue (black) are (are not) assimilated in CORA.

Additionally, CORA-derived and gauge-derived HTF predictions were skillful at nearly all the same stations using the metric of Dusek et al. (2022; Fig. 6). Across the considered flood

thresholds, CORA-derived HTF predictions were skillful at 94% of the stations for which gauge-derived predictions were also skillful, while there were an additional six instances where CORA-derived HTF predictions were skillful but those from the gauge were not. For the stations where gauge-derived predictions were skillful, those from CORA were also skillful at 58/58, 54/57, 35/41, and 20/21 stations (20/20 for stations with at least 10 floods) for the considered flood thresholds in increasing order (Fig. 6a-d). This result also indicates that HTF model performance decreased with increasing flood threshold; fewer stations were skillful for both gauge and CORA input as flood threshold increased. The greatest loss of skillfulness for CORA input, in terms of BSS, was in the MA and Gulf regions (Fig. 6a-d).

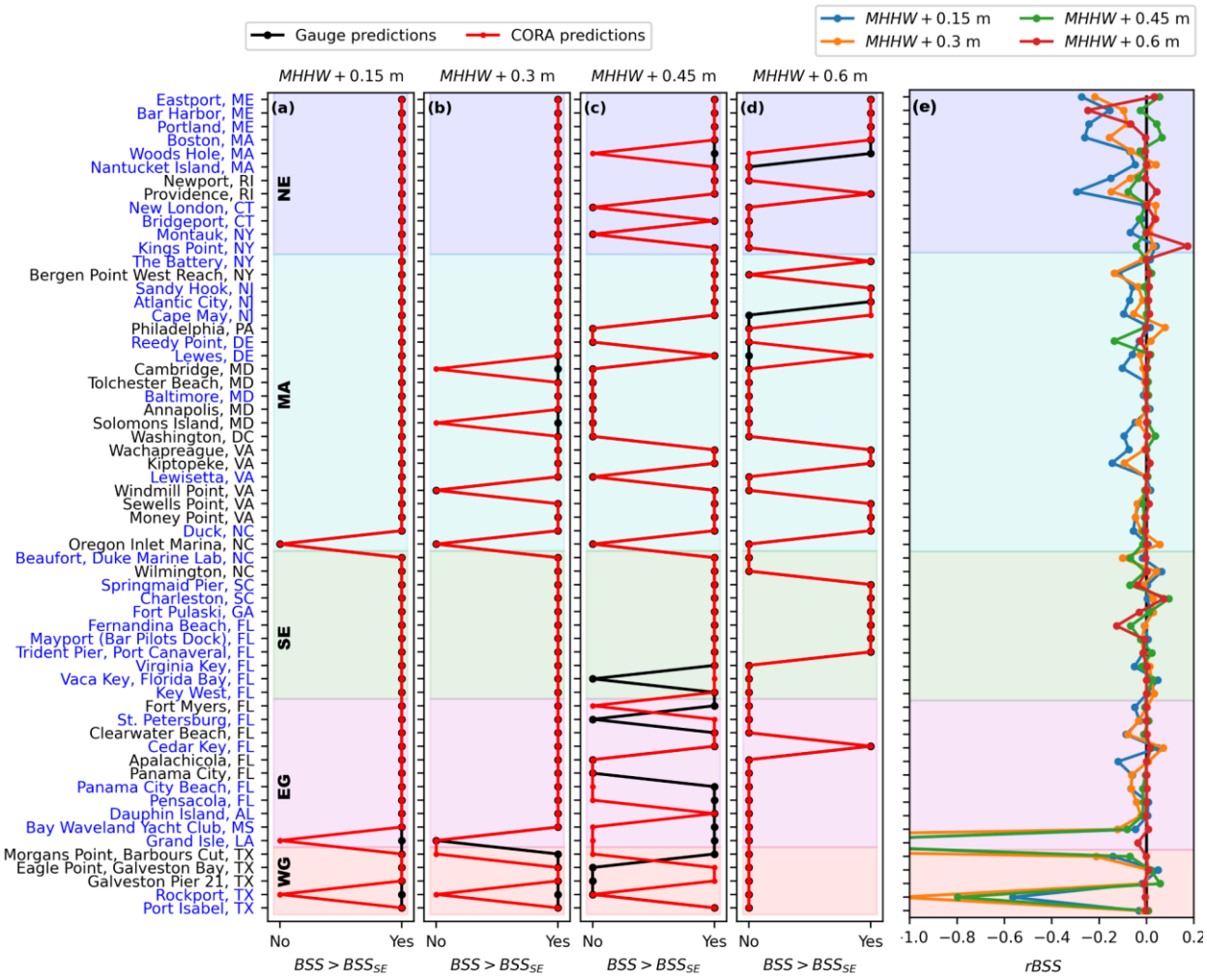

Fig. 6. Brier Skill Score comparisons for CORA- and gauge-derived HTF predictions. (a-d) Comparison, at one-month lead, of stations that obtain a Brier Skill Score (BSS) that is greater than the standard error of

the BSS as computed following Bradley et al. (2008) for both gauge-derived (black) and CORA-derived (red) high tide flooding predictions for flood thresholds of (a) $MHHW + 0.15$ m, (b) $MHHW + 0.30$ m, (c) $MHHW + 0.45$ m, and (d) $MHHW + 0.60$ m. (e) $rBSS$, interpretable as the proportional performance change in terms of Brier Score when using CORA as input relative to using gauge data as input, for all stations and flood thresholds considered at one-month lead. The geographic regions (see Fig. 1) are shown by the shading and labeled. Station names written in blue (black) are (are not) assimilated in CORA.

Summarizing these differences in BSS using the $rBSS$ (Fig. 6e), performance of the HTF model declined by just 2% ($rBSS = -0.02$) on average across regions and thresholds when CORA was used instead of gauge data. $|rBSS|$ was inversely proportional to flood threshold, with average values of -0.05 for $MHHW + 0.15$ m, -0.03 for $MHHW + 0.30$ m, -0.01 for $MHHW + 0.45$ m, and 0.00 for $MHHW + 0.60$ m. Across flood thresholds, 91% of the 236 total datapoints obtained $|rBSS| \leq 0.10$. 39% obtained $rBSS > 0$, i.e. an increase in HTF model performance for CORA input relative to gauge input.

The ROC curves also confirmed that CORA-derived HTF predictions were quite similar to those from the gauges, with the curves from CORA and gauge typically lying nearly atop one another (Fig. 7a-d). The average reduction in AUC for CORA input was only 1% as compared to gauge input (Fig. 7e). AUC reductions for all regions and thresholds were $\leq 4\%$ except in the EG for $MHHW + 0.30$ m (7%). Similar to the CRPS (Fig. 5) and BSS (Fig. 6) analyses, there were instances for which HTF model performance was stronger (larger AUC) for CORA input than gauge input, particularly for a HTF threshold of $MHHW + 0.45$ m (Fig. 7a-d). Similar to the BSS analysis (Fig. 6a-d), HTF model performance as a whole decreased as the flood threshold increased, with ROC curves becoming closer to the 1:1 random guess line (Fig. 7a-d). Further, for all HTF thresholds model performance for both CORA and gauge input was highest in the NE, lower in the MA and SE, and weakest in the Gulf regions.

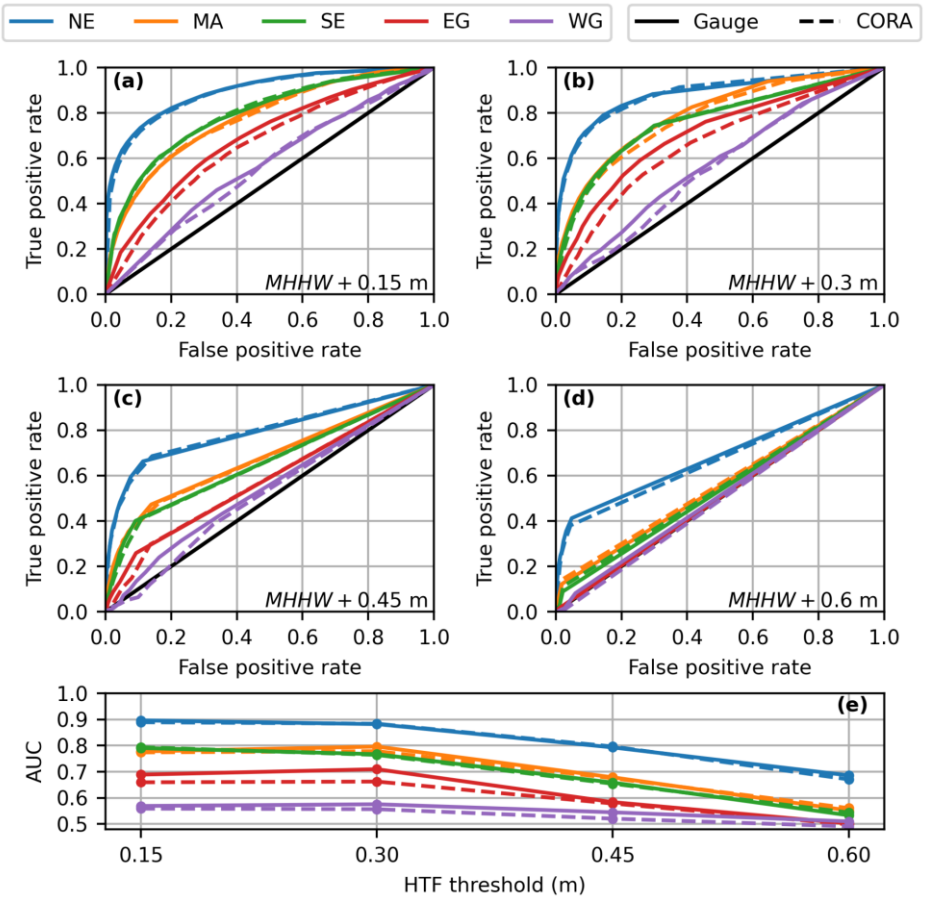

Fig. 7. Receiver Operating Characteristic (ROC) curves and area under the curves (AUC) at one month lead for gauge-derived and CORA-derived predictions of high tide flooding. (a-d) ROC curves for flood thresholds of (a) $MHHW + 0.15$ m, (b) $MHHW + 0.30$ m, (c) $MHHW + 0.45$ m, and (d) $MHHW + 0.60$ m. (e) AUC for each curve. Note that AUC=1 indicates perfect predictions, while a random guess obtains AUC=0.5.

4.3. Case study near Charleston, S.C.

A demonstration of the value of CORA-derived HTF predictions was performed near Charleston, S.C. for two spatial scales at a flood threshold of $MHHW + 0.60$ m (Fig. 8). HTF predictions were made around two adjacent barrier islands (Fig. 8b) and between the neighboring NWLON stations of Charleston and Fort Pulaski (Fig. 8c). Note that, for this flood threshold, HL agreement is >98% and HL bias is ≤0.01 at these stations (Fig. 4a,b).

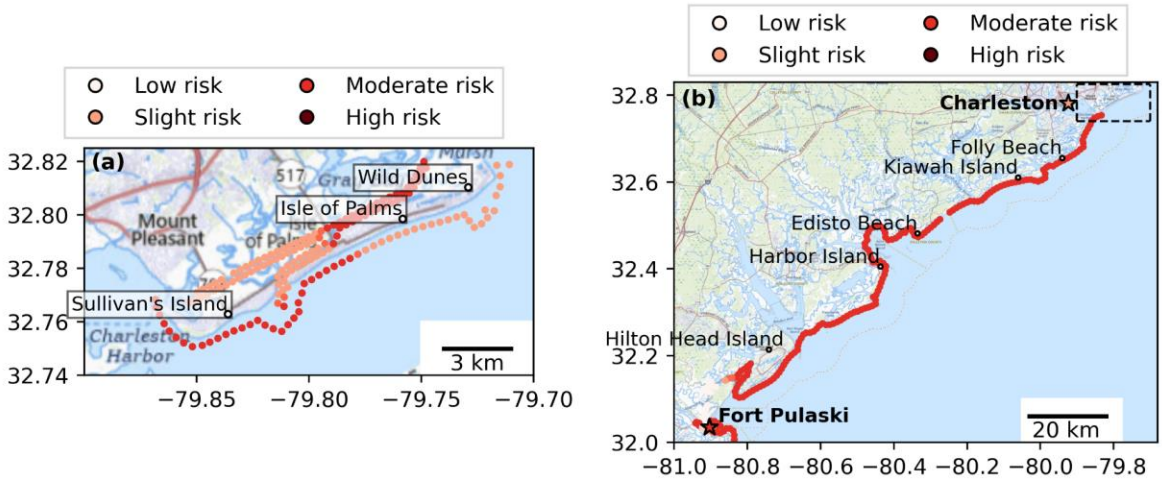

Fig. 8. Demonstration of spatially continuous predictions of risk of high tide flooding above $MHHW + 0.60$ m ($MHHW + 2$ ft) at one-month lead time using CORA on October 19, 2020 near Charleston, SC. (a) HTF hazard level predictions around two barrier islands using a 5-point nearest neighbor smoothing. (b) HTF hazard level predictions for the coastline between the Fort Pulaski and Charleston tide gauges using a 5-point nearest neighbor smoothing, with predictions from the tide gauges shown as stars. In (b), the dashed box shows the spatial area of (a). The hazard levels have the following HTF probability bounds: low: 0-20%, slight: 20-40%, moderate: 40-60%, high: 60-100%. Map source: USGS National Map.

Both applications illustrate spatial variability in HTF risk that is not observable using tide gauges alone. For example, certain bay- and ocean-facing sides of the barrier islands were predicted to obtain different HLs on this day (Fig. 8b), as could be expected based on hydrodynamic differences around a barrier island driven by patterns in bathymetry, wave dissipation, constrictions to exchange, and shoreline orientation (e.g. Cañizares & Irish, 2008; Sherwood et al., 2014; Smallegan et al., 2017). Similarly, all ocean-facing locations between the Charleston and Fort Pulaski tide gauges were predicted to obtain the same HL as the Fort Pulaski gauge, even those that lie closer to the Charleston gauge (Fig. 8c). The difference at ocean-facing locations near Charleston may result from the gauge's inland position within the harbor, which modifies tidal and water level dynamics relative to the open coast. This localized HTF guidance could help these communities more effectively focus resources when preparing for potential flooding events, rather than having to rely on the nearest tide gauge which may be 10s of km away and/or in an area with considerably different morphodynamics.

5. Discussion

Our results indicate that there was minimal change in HTF predictions at NWLON stations when CORA was used in place of gauge observations. Average reduction in HTF model performance was just 5% using the CRPS (Fig. 5), 2% using the $rBSS$ (Fig. 6e), and 1% using the AUC (Fig. 7). Additionally, CORA yielded the same HL as the gauge at least 77% of the time on average for each flood threshold, with greater agreement at the highest considered flood thresholds (Fig. 4, Table 1). This minimal performance change translated to similar, though not identical, stations that were skillful when using CORA as compared to gauge observations: stations that were skillful using gauge observations were also skillful using CORA for 94% of cases across the considered flood thresholds (Fig. 6a-d). Additionally, it is noteworthy that CORA and gauge input both yielded the same pattern of decreasing HTF model performance with increasing flood threshold (Figs. 5,6), as also documented in Dusek et al. (2022). This pattern is because, at higher flood thresholds, the tidal contribution to floods is relatively small, and there are fewer floods overall on which to assess model skill in terms of flood days.

The minimal HTF model skill reduction of $\leq$5% on average for CORA-based HTF predictions using three different statistical metrics yields some confidence that CORA can provide spatially-continuous HTF guidance away from the stations. Considering the accuracy metrics at only the stations not assimilated in CORA (those with names in black in Figs. 3-5) provides a proxy for performance away from the gauges. In particular, since unassimilated stations are located in non-open coast environments (Keeney et al., 2025; Fig. 1), accuracy at unassimilated stations may be somewhat representative of accuracy specifically in these environments. The comparison between CORA-derived and gauge-derived HTF predictions at unassimilated stations was similar to assimilated stations. For example, the change in CRPS at the unassimilated stations was 6%, similar to that at assimilated stations of 4% (5% overall; Fig.

5). Additionally, HL agreement at unassimilated stations was, on average, within 10% of that at assimilated stations for all flood thresholds considered, at 80%, 87%, 96%, and 99% for the flood thresholds in increasing order at assimilated stations, and 73%, 78%, 96%, and 100% at unassimilated stations (Fig. 4). Finally, of the eight stations which were skillful using gauge input but not for CORA input for at least one flood threshold, four were assimilated and four were not (Fig. 6).

While the comparison between CORA-derived and gauge-derived HTF predictions at the NWLON stations indicates minimal performance change overall, there is variability as a function of region and HTF threshold. For example, the Gulf regions showed the greatest decrease in number of stations that were mutually skillful as the flood threshold increased (Fig. 6). The EG also obtained the maximum single-threshold AUC reduction for any region or threshold at 7%, as well as the largest region-averaged reduction in CRPS at 8%. It is noteworthy that there are known limitations to CORA in the Gulf: available data from NWLON stations to drive the data assimilation are particularly scarce here (see Fig. 23 in Keeney et al., 2025), causing water level errors relative to typical variability to be especially large (see Fig. 27 in Keeney et al., 2025). Indeed, the WG has only four comparison stations, of which only one is assimilated in CORA (Table 1; S3 Table; see also Figures 4-6). Additionally, there are Gulf locations with relatively large local rates of land subsidence (such as Eagle Point, T.X.; Qiao et al., 2023), which CORA cannot capture at unassimilated locations. Grand Isle and Rockport in particular (S4 Appendix), as well as the difference in trend at Eagle Point (Fig. 2c), highlight these inaccuracies in CORA.

The variations in the comparison between CORA- and gauge-derived HTF predictions as a function of region and threshold are also partially due to interacting biases between the HTF model and CORA over different flood thresholds. At Philadelphia, for example (Fig. 9a), CORA-derived HTF probabilities tend to be slightly higher than those from the gauge (HL biases

of 0.29, 0.24, 0.01, 0.00 for the four flood thresholds in increasing order; Fig. 4b). This high bias for CORA somewhat counteracted a structural underprediction of the HTF model- due to its inability to capture weather driven flooding (Dusek et al. 2022)- and caused the station to have a smaller CRPS for CORA input (Fig. 5) and a positive or zero $rBSS$ for all flood thresholds (Fig. 6e). This helps explain how some stations achieved stronger model performance for CORA input. For the example of Boston (Fig. 9b), however, where CORA-derived HTF probabilities tended to be similarly high-biased, HTF probabilities were so large during peak events that the high-bias only contributed to increasing errors during periods of high predicted probability without an observed flood (Fig. 9b). This helps explain the relatively large performance degradation in terms of $rBSS$ and CRPS in the NE, particularly for lower flood thresholds (Figs 4,5e). Slight differences in methods for the computation of physical quantities for gauges vs. CORA (e.g. datums, tide predictions, and long-term trends; Figure 2) could also explain some differences in HTF predictions.

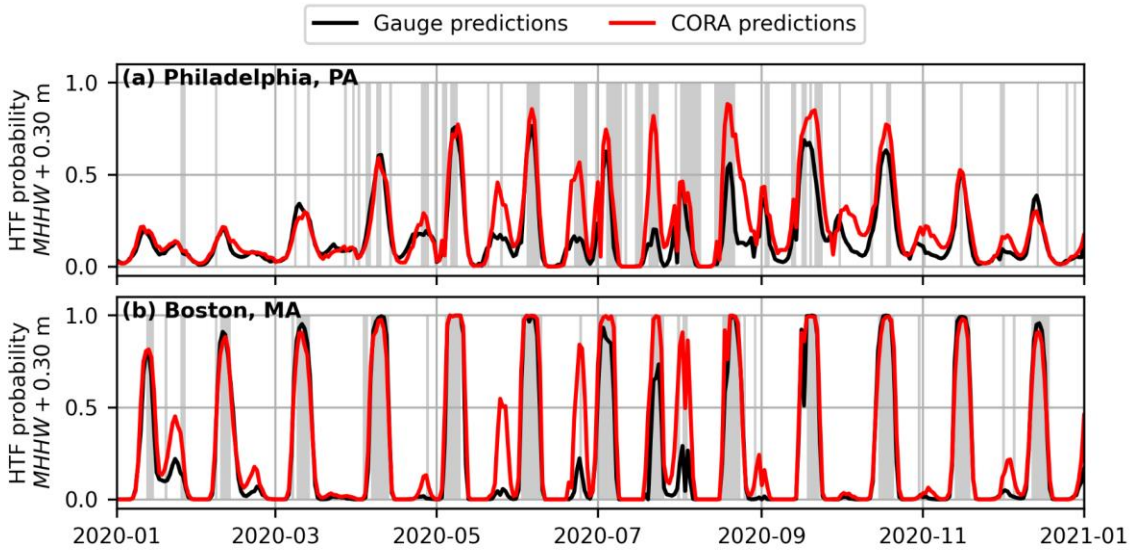

Fig. 9. Comparison of HTF predictions and observations above $MHHW + 0.30$ m for Philadelphia, P.A. (a) and Boston, M.A. (b). Observed floods are indicated by gray shading. Only observations and HTF predictions for 2020 are shown for visualization purposes; predictions were made for 2020 through 2022.

6. Towards an operational community-level HTF outlook

By documenting minimal change in HTF predictions and skill using CORA at the NWLON stations and demonstrating the potential output and value of localized HTF predictions near Charleston, S.C., this work lays the foundation for an operational spatially continuous monthly HTF outlook that can provide localized flood likelihoods nationwide. A number of outstanding questions remain in order to scale these results to a national operational product. Most importantly, the current methodology and data do not support real-time predictions, as the HTF model requires water level observations up to and including the month before HTF predictions are to be made so that damped persistence values can be computed and prediction lead times are small (Dusek et al., 2022; see Section 2.2). More frequent, monthly to yearly updates of CORA, similar to other ocean and atmosphere reanalyses (e.g. ERA5; Hersbach et al., 2020) would be perhaps the simplest approach to allow real-time predictions. Alternative approaches could also be pursued with the existing CORA data, such as developing relationships between CORA nodes and tide gauges for the time period covered by CORA, either through statistical or machine-learning approaches, and extending these to real-time predictions. Further research could focus on this topic. Relatedly, efforts are ongoing to replace the sea level persistence in the HTF model with downscaled climate model output (Albers et al., 2025), which could provide further flexibility for real-time predictions.

Further, the comparison at NWLON stations, even at those that are not assimilated in CORA, does not provide a fully comprehensive understanding of CORA-derived HTF prediction accuracy in all relevant coastal locations and morphodynamic environments. For example, even though non-assimilated stations are in non-open coast environments, they do not sample back-barrier locations or locations very far up rivers, leaving the accuracy of CORA-derived HTF predictions in these environments technically unknown. While potential validation data in these and other environments is inherently limited by a lack of observations (hence the need for

CORA), non-NWLON tide gauge networks such as those recently available through Hohonu Inc. (Fiorentino et al., 2025) as well as supporting data such as media reports of flooding occurrences could be used to more fully assess CORA-derived HTF prediction accuracy at new locations in future work. Additionally, a more bottom-up approach could be an analysis of pre- and post-assimilated CORA output to deduce a more robust understanding of the spatially variable effects of the data assimilation as a function of morphodynamic environment and/or distance from NWLON stations. The 400-500 m resolution of CORA is also an important consideration: it is possible that narrow waterways such as back-barrier bays and inland estuaries with hydrodynamics varying on spatial scales of O(1-10 m) may not be captured sufficiently or at all by CORA, leaving HTF predictions not possible in these locations. Improving the spatial resolution in future CORA versions could help alleviate this limitation. Even if sampled, however, such environments may not be inundated at all times and are likely very shallow, which could drive nonlinear interactions between water level components that result in strongly non-Gaussian distributions (e.g. Aubrey & Speer, 1985). Since the HTF model was developed for always-inundated tide gauge data, we here limited the application to CORA nodes that were (nearly) never dry. Further research is needed to develop methods to handle intermittently dry data and further explore possible non-Gaussian distributions in these shallow CORA locations. Indeed, it has recently been shown that non-Gaussian stochastically generated skewed distributions may better characterize non-tidal residuals than Gaussian distributions at NWLON stations (Hovenga et al., 2025).

A further challenge for a national-scale product will be the delineation of a reliable and useful shoreline-following subset of CORA points at which to deliver HTF predictions at a national scale.. The two techniques applied at prototype-scale in this work- tracing points delineating the boundary of always/not always wet nodes (Fig. 9b) and utilizing a buffer from a shoreline model (Fig. 9c)- are promising. However, these approaches will likely require manual

refinement or additional local considerations at a larger scale; for example around the highly complex coastlines of Maine and the Mississippi River delta. Other approaches could also be viable, such as tracing a depth contour for nodes that are inundated a certain percentage of the time, and further research is needed on this topic.

Finally, it will be useful to provide uncertainty bounds on HTF predictions, as this helps convey input and model uncertainties to potentially non-expert end users. We have explored a method to propagate uncertainty in CORA water levels, which are on the order of 0.10-0.15 m (Keeney et al., 2025), to CORA-derived HTF predictions. The method is based on a Monte Carlo approach, wherein many realizations of model predictions are generated when randomly sampling model parameters from a probability distribution capturing their uncertainties (e.g. Zhang et al., 2021 and the references therein). Using observed error distributions in CORA water levels and tide predictions, an ensemble of possible HTF predictions can be made by varying CORA values within these distributions (e.g. Fig. 10 red area). For example, by examining CORA vs. observed NTR, Eq. (1) can be modified as:

$$\mu_{clim}(t) = \mu_{month}(t) + \mu_{tide}(z) + p(t) \pm \delta_{NTR}, \quad (7)$$

where δ_{NTR} is a random value between 0 and the standard deviation of the CORA NTR errors. The modified value of $\mu_{clim}(t)$ is then compared with the distance between the flood threshold and predicted tide similarly modified within the standard deviation of the CORA tide prediction errors δ_{tide}. Comparing to Fig. 3c, it is clear that while deterministic CORA-derived HTF predictions are often higher than those derived from the gauge for this example, the (temporally-varying) uncertainty range on CORA-derived HTF predictions always encompasses the gauge predictions (Fig. 10). For example, for the high probability event at the beginning of July 2022, gauge-derived HTF probability is 0.94, while the bounds of CORA-derived HTF probability are

0.60-0.99 (Fig. 10). This approach could provide a useful method for delivering probabilistic HTF predictions with uncertainty estimates. However, the iterative nature of the method is relatively inefficient, and other approaches should also be investigated to facilitate application at the many thousands of possible CORA nodes.

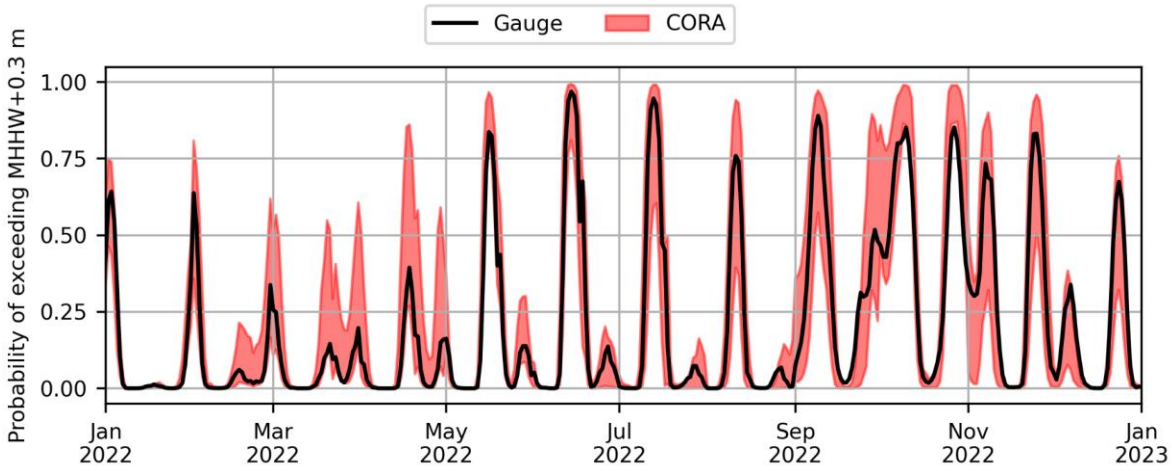

Fig. 10. CORA-derived high tide flooding probability uncertainty bounds above $MHHW + 0.30$ m (red) for the Charleston NWLON station at one month lead in comparison to gauge-derived predictions (black). Uncertainty bounds show the 25th-75th percentile of a 20-member ensemble. Only predictions for 2022 are shown for visualization purposes; predictions were made for 2020 through 2022.

7. Conclusions

The existing monthly HTF outlook, delivered only at NWLON stations, is an important tool to help local planners time the allocation of response staff and resources to areas with the highest flood risk. This work lays the foundation for a spatially-continuous monthly HTF outlook every 400-500 m using CORA by demonstrating minimal change in HTF predictions when CORA is used in place of gauge observations at NWLON stations, including those that are not assimilated in CORA, and illustrating cases of variable CORA-derived flood likelihoods along the coast not observable using gauges. While further research is needed to more comprehensively understand the accuracy of CORA-derived predictions in all relevant locations and morphodynamic environments, and challenges remain for scaling these results to a national

operational product, a spatially continuous monthly HTF outlook will provide critical localized information to communities and empower more effective flood preparation and mitigation.

Acknowledgements

The authors wish to thank the many individuals who contributed to the development of CORA, particularly those at the University of North Carolina's Renaissance Computing Institute and Tetra Tech/RPS. The authors also wish to thank two anonymous reviewers whose comments improved the quality of the manuscript.

References:

Albers JR, Newman M, Balmaseda M, Sweet WV, Wang Y, Xu T. Assessing Subseasonal Forecast Skill for Use in Predicting US Coastal Inundation Risk [Preprint]. ESS Open Archive. 2025. Available from: https://doi.org/10.22541/essoar.173809913.37896968/v1

Aubrey, D. G., and Speer, P.E. A study of non-linear tidal propagation in shallow inlet/estuarine systems Part I: Observations. Est. Coast. and Shelf Sci. 1985; 21(2): 185-205. https://doi.org/10.1016/0272-7714(85)90096-4

Bradley AA, Schwartz SS, Hashino T. Sampling uncertainty and confidence intervals for the Brier score and Brier skill score. Weather Forecasting. 2008;23:992–1006. https://doi.org/10.1175/2007WAF2007049.1

Burgos AG, Hamlington BD, Thompson PR, Ray RD. Future nuisance flooding in Norfolk, VA, from astronomical tides and annual to decadal internal climate variability. Geophys Res Lett. 2018;45(22):12432. https://doi.org/10.1029/2018GL079572

Codiga DL. Unified tidal analysis and prediction using the UTide Matlab functions. GSO Tech Rep. 2011;2011-01.

Dahl KA, Fitzpatrick MF, Spanger-Siegfried E. Sea level rise drives increased tidal flooding frequency at tide gauges along the US East and Gulf Coasts: Projections for 2030 and 2045. PLoS One. 2017;12(2):e0170949. https://doi.org/10.1371/journal.pone.0170949

Dusek G, Loesch R, Stone P, Heilman L, Fiorentino L. National Water Level Observation Network (NWLON) Requirement. NOAA Tech Rep NOS CO-OPS. 2024;(107). https://doi.org/10.25923/h9h9-6p20

Dusek G, Sweet WV, Widlansky MJ, Thompson PR, Marra JJ. A novel statistical approach to predict seasonal high tide flooding. Front Mar Sci. 2022;9:1073792. https://doi.org/10.3389/fmars.2022.1073792

Egbert, G. D., Erofeeva, S. Y. Efficient inverse modeling of barotropic ocean tides. J Atmos Ocean Tech. 2002;*19*(2):183-204. https://doi.org/10.1175/1520-0426(2002)019<0183:EIMOBO>2.0.CO;2

Fant C, Jacobs JM, Chinowsky P, Sweet W, Weiss N, Sias JE, et al. Mere nuisance or growing threat? The physical and economic impact of high tide flooding on US road networks. J Infrastruct Syst. 2021;27(4):04021044. https://doi.org/10.1061/(ASCE)IS.1943-555X.0000652

Fiorentino, L., Dusek, G., & Pe'eri, S. Estimating total vertical uncertainty of short term and partner water level observations. NOAA Tech Report NOS CO-OPS 112; 2025. https://doi.org/10.25923/s9h7-vy98

Goodman AC, Thorne KM, Buffington KJ, Freeman CM, Janousek CN. El Niño increases high-tide flooding in tidal wetlands along the U.S. Pacific Coast. J Geophys Res Biogeosci. 2018;123:3162–77. https://doi.org/10.1029/2018JG004677

Hersbach H, Bell B, Berrisford P, Hirahara S, Horányi A, Muñoz-Sabater J, et al. The ERA5 global reanalysis. Q J R Meteorol Soc. 2020;146(730):1999–2049. https://doi.org/10.1002/qj.3803

Hino M, Belanger ST, Field CB, Davies AR, Mach KJ. High-tide flooding disrupts local economic activity. Sci Adv. 2019;5:eaau2736. https://doi.org/10.1126/sciadv.aau2736

Hovenga, P., Newman, M., Albers, J.R., Sweet, W., Dusek,, G., Xu, T., Callahan, C., Shin, S. Using stochastically generated skewed distributions to represent hourly nontidal residual water levels at United States tide gauges. Frontiers in Mar. Sci. 2025;12:1618367. https://doi.org/10.3389/fmars.2025.1618367

Hummel MA, Berry MS, Stacey MT. Sea level rise impacts on wastewater treatment systems along the U.S. coasts. Earth's Future. 2018;6:622–33. https://doi.org/10.1002/2017EF000805

Jacobs JM, Cattaneo LR, Sweet W, Mansfield T. Recent and future outlooks for nuisance flooding impacts on roadways on the U.S. East Coast. Transp Res Rec. 2018;2672:1–10. https://doi.org/10.1177/0361198118756366

Kavanaugh K, Keeney A, Callahan J, Sweet W. Notice of Methodology Update: NOAA High Tide Flooding Outlooks. NOAA Technical Service Publication NOS CO-OPS 001; 2023. https://tidesandcurrents.noaa.gov/publications/HTF_Notice_of_Methodology_Update_2023.pdf

Keeney A, Dusek G, Callahan J, Ratcliff J, Jima T, Brooks W, Marcy D, et al. NOAA's Coastal Ocean Reanalysis: Gulf of Mexico, Atlantic, and Caribbean. NOAA Tech Rep NOS CO-OPS 108; 2025. https://doi.org/10.25923/5ypp-4e84

Li S, Wahl T, Barroso A, Coats S, Dangendorf S, Piecuch C, et al. Contributions of different sea-level processes to high-tide flooding along the US Coastline. J Geophys Res Oceans. 2022;127(7):e2021JC018276. https://doi.org/10.1029/2021JC018276

Lictae L, Huang L, Dusek G. A Comparison of Datums Derived from CO-OPS Verified Data Products and Tidal Analysis Datum Calculator. NOAA Tech Rep NOS CO-OPS 085; 2017.

Little CM, Hu A, Hughes CW, McCarthy GD, Piecuch CG, Ponte RM, Thomas MD. The relationship between US East Coast sea level and the Atlantic meridional overturning circulation: A review. J Geophys Res Oceans. 2019;124(9):6435–58. https://doi.org/10.1029/2019JC015152

Mason SJ, Graham NE. Areas beneath the relative operating characteristics (ROC) and relative operating levels (ROL) curves: Statistical significance and interpretation. Q J R Meteorol Soc. 2002;128(584):2145–66. https://doi.org/10.1256/003590002320603584

Mason SJ, Graham NE. Conditional probabilities, relative operating characteristics, and relative operating levels. Weather Forecast. 1999;14(5):713–25. https://doi.org/10.1175/1520-0434(1999)014<0713:CPROCA>2.0.CO;2

May CL, Osler MS, Stockdon HF, Barnard PL, Callahan JA, Collini RC, et al. Ch. 9. Coastal effects. In: Crimmins AR, Avery CW, Easterling DR, Kunkel KE, Stewart BC, Maycock TK, editors. Fifth National Climate Assessment. Washington, DC: U.S. Global Change Research Program; 2023. https://doi.org/10.7930/NCA5.2023.CH9

McAlpine SA, Porter JR. Estimating recent local impacts of sea-level rise on current real-estate losses: A housing market case study in Miami-Dade, Florida. Popul Res Policy Rev. 2018;37:871–95. https://doi.org/10.1007/s11113-018-9473-5

Miller A, Luscher A. NOAA's national water level observation network (NWLON). J Oper Oceanogr. 2019;12(sup2):S57–66. https://doi.org/10.1080/1755876X.2018.1523301

Moftakhari H, Aghakouchak A, Sanders BF, Matthew RA, Mazdiyasni O. Translating uncertain sea level projections into infrastructure impacts using a Bayesian framework. Geophys Res Lett. 2017;44:11914–21. https://doi.org/10.1002/2017GL076116

National Weather Service Climate Prediction Center. U.S. Week 2 Hazards Outlook [Internet]. 2025 [cited 2025 May 27]. Available from: https://www.cpc.ncep.noaa.gov/products/predictions/threats/threats.php

NOAA CO-OPS. CORA-Coastal-Ocean-Reanalysis-CORA [Source code]. GitHub; 2025 [cited 2025 May 27]. Available from: https://github.com/NOAA-CO-OPS/CORA-Coastal-Ocean-Reanalysis-CORA

NOAA CO-OPS. Seasonal_High_Tide_Flooding_Prediction [Source code]. GitHub; 2024 [cited 2025 May 27]. Available from: https://github.com/NOAA-CO-OPS/Seasonal_High_Tide_Flooding_Prediction

NOAA National Geodetic Survey. Continually Updated Shoreline Product [Data set]. NOAA Digital Coast; 2025 [cited 2025 May 27]. Available from: https://coast.noaa.gov/digitalcoast/data/cusp.html

NOAA's National Ocean Service, The Center for Operational Oceanographic Products and Services. NOAA's Coastal Ocean Reanalysis (CORA) Dataset [Internet]. [cited 2025 May 27]. Available from: https://registry.opendata.aws/noaa-nos-cora/

National Oceanic and Atmospheric Administration. Annual High Tide Flooding Outlook [Internet]. [cited 2025 May 27]. Available from: https://tidesandcurrents.noaa.gov/high-tide-flooding/annual-outlook.html

National Oceanic and Atmospheric Administration. Monthly High Tide Flooding Outlook [Internet]. 2025 Mar 10 [cited 2025 May 27]. Available from: https://tidesandcurrents.noaa.gov/high-tide-flooding/monthly-outlook.html

Obeysekera J, Irizarry M, Park J, Barnes J, Dessalegne T. Climate change and its implications for water resources management in south Florida. Stoch Environ Res Risk Assess. 2011;25:495–516. https://doi.org/10.1007/s00477-010-0418-8

Parker A, Ollier CD. Short-term tide gauge records from one location are inadequate to infer global sea-level acceleration. Earth Syst Environ. 2017;1:1–10. https://doi.org/10.1007/s41748-017-0019-5

Parker B. Tidal Analysis and Prediction. NOAA Special Publication NOS CO-OPS 3. 2007.

Piecuch CG, Das SB, Gorrell L, Dangendorf S, Hamlington BD, Thompson PR, Wahl T. Impacts-Based Thresholds for Investigation of High-Tide Flooding in the United States. Earth's Future. 2025;13(4). https://doi.org/10.1029/2024EF003959

Qiao, X., Chu, T., Tissot, P., & Holland, S. Long-term vertical-land-motion investigation with space and terrestrial geodetic techniques near San Leon, Texas, USA. Int. J. App. Earth Obs. And Geoinf. 2023;*125*:103580.

Rose L, Widlansky MJ, Feng X, Thompson P, Asher TG, Dusek G, et al. Assessment of water levels from 43 years of NOAA's Coastal Ocean Reanalysis (CORA) for the Gulf of Mexico and East Coasts. Front Mar Sci. 2024;11:1381228. https://doi.org/10.3389/fmars.2024.1381228

Sun Q, Dangendorf S, Wahl T, Thompson PR. Causes of accelerated High-Tide Flooding in the US since 1950. Nat Clim Atmos Sci. 2023;6(1):210. https://doi.org/10.1038/s41612-023-00538-5

Sweet WV, Dusek G, Obeysekera JTB, Marra JJ. Patterns and projections of high tide flooding along the US coastline using a common impact threshold. NOAA Technical Report NOS CO-OPS 086. 2018.

Sweet WV, Hamlington BD, Kopp RE, Weaver CP, Barnard PL, Bekaert D, Brooks W, et al. Global and regional sea level rise scenarios for the United States: Updated mean projections and extreme water level probabilities along U.S. coastlines. NOAA Technical Report NOS 01. 2022.

Sweet WV, Simon S, Dusek G, Marcy D, Brooks W, Pendleton M, et al. 2021 state of high tide flooding and annual outlook. NOAA High Tide Flooding Report. 2021.

Thompson PR, Hamlington BD, Landerer FW, Adhikari S. Are long tide gauge records in the wrong place to measure global mean sea level rise? Geophys Res Lett. 2016;43(19):10403. https://doi.org/10.1002/2016GL070552

Thompson PR, Widlansky MJ, Hamlington BD, Merrifield MA, Marra JJ, Mitchum GT, Sweet W. Rapid increases and extreme months in projections of United States high-tide flooding. Nat Clim Chang. 2021;11(7):584–90. https://doi.org/10.1038/s41558-021-01077-8

Tsimplis MN, Woodworth PL. The global distribution of the seasonal sea level cycle calculated from coastal tide gauge data. J Geophys Res Oceans. 1994;99(C8):16031–9. https://doi.org/10.1029/94JC01115

Vandenberg-Rodes A, Moftakhari HR, AghaKouchak A, Shahbaba B, Sanders BF, Matthew RA. Projecting nuisance flooding in a warming climate using generalized linear models and Gaussian processes. J Geophys Res Oceans. 2016;121(11):8008–20. https://doi.org/10.1002/2016JC012084

Wilks DS. Statistical methods in the atmospheric sciences. Vol. 100. 3rd ed. Amsterdam: Academic Press; 2011.

Zervas C. Sea level variations in the United States, 1854–2006. NOAA Technical Report NOS CO-OPS 053. 2009.

Zhang J. Modern Monte Carlo methods for efficient uncertainty quantification and propagation: A survey. Wiley Interdiscip Rev Comput Stat. 2021;13(5):e1539. https://doi.org/10.1002/wics.1539

Supporting Information:

S1 Appendix. CORA-derived vs. gauge-derived HTF predictions at three-month lead.

The accuracy of CORA-derived HTF predictions was very similar at three month lead as at one month lead. For example, values of HL agreement, bias, and MAE at three month lead were nearly all identical to those at one month lead (compare Table S1 to Table 1). Using the CRPS, performance of the HTF model declined when CORA input was used instead of gauge data by the same amount at three month lead as at one month lead (5%). Further, on average across the considered flood thresholds, CORA-derived HTF predictions were skillful at nearly the same proportion of stations for which gauge-derived predictions were also skillful at three month lead (96%) as at one month lead (94%). Additionally, performance of the HTF model in terms of BSS declined by the same amount when CORA was used instead of gauge data at three month lead as at one month lead (2%). Finally, reduction in AUC for CORA input was nearly the same at three month lead (2%) as at one month lead (1%).

Table S1. Average values of HL agreement, bias, and MAE, respectively, within each region and for each flood threshold at three month lead.

Region	$MHHW + 0.15$ m	$MHHW + 0.30$ m	$MHHW + 0.45$ m	$MHHW + 0.60$ m	**mean**
NE	76% | 0.22 | 0.29	87% | 0.11 | 0.16	94% | 0.01 | 0.07	97% | -0.01 | 0.03	**89% | 0.08 | 0.14**
MA	79% | 0.14 | 0.23	82% | 0.08 | 0.19	98% | 0.01 | 0.03	100% | 0.00 | 0.00	**90% | 0.06 | 0.11**
SE	81% | 0.07 | 0.20	90% | 0.04 | 0.11	97% | 0.00 | 0.03	100% | 0.00 | 0.00	**92% | 0.03 | 0.08**
EG	77% | 0.02 | 0.25	85% | 0.01 | 0.16	98% | 0.01 | 0.02	100% | 0.00 | 0.00	**90% | 0.01 | 0.11**
WG	68% | -0.10 | 0.36	63% | -0.29 | 0.49	85% | -0.12 | 0.18	99% | -0.01 | 0.01	**79% | -0.13 | 0.26**
mean	**76% | 0.07 | 0.27**	**81% | -0.01 | 0.22**	**94% | -0.02 | 0.07**	**99% | 0.00 | 0.01**	

S2 Table. Overview of all GEC NWLON stations and those used in this study.

Tide Gauge Station ID	Station Name	State	Data Start Year	Data End Year	Missing data from 1997-2023	Notes
8410140	Eastport	ME	1929	Today	None	Not used in Dusek et al. (2022)
8411060	Cutler Farris Wharf	ME	2010	Today		
8413320	Bar Harbor	ME	1947	Today	Jan 1998-Jul 1999, Dec 1999-Aug 2000, Oct 2000-Jun 2001	
8418150	Portland	ME	1910	Today	None	
8419870	Seavey Island	ME	2020	Today		
8443970	Boston	MA	1921	Today	None	
8447386	Fall River	MA	1999	Today	None	
8447435	Chatham	MA	2009	Today		
8447636	New Bedford Harbor	MA	2023	Today		
8447930	Woods Hole	MA	1958	Today	End 2007-beginning 2008	
8449130	Nantucket Island	MA	1965	Today	None	
8452660	Newport	RI	1930	Today	None	
8452944	Conimicut Light	RI	1999	Today	None	
8454000	Providence	RI	1938	Today	None	
8454049	Quonset Point	RI	1999	Today	Mid 1999 - mid 2000	
8461490	New London	CT	1938	Today	None	
8465705	New Haven	CT	1999	Today	None	
8467150	Bridgeport	CT	1970	Today	None	
8510560	Montauk	NY	1947	Today	None	
8516945	Kings Point	NY	1998	Today	Jan 1997-Nov 1998	
8518750	The Battery	NY	1920	Today	June 1997-Nov 1997, Jan 2001-May 2001, Feb 2004-Jun 2004	
8519483	Bergen Point West Reach	NY	1981	Jan 2024	Dec 2009-Mar 2010	
8531680	Sandy Hook	NJ	1910	Today	None	
8534720	Atlantic City	NJ	1911	Today	Dec 2001-May 2002	
8536110	Cape May	NJ	1965	Today	Dec 2002 - Apr 2003	
8537121	Ship John Shoal	NJ	2002	Today		
8539094	Burlington, Delaware River	NJ	2002			
8540433	Marcus Hook	PA	2002	Today		
8545240	Philadelphia	PA	1989	Today	None	
8546252	Bridesburg	PA	2016	Today		
8548989	Newbold	PA	2001	Today		
8551762	Delaware City	DE	2001	Today	None	
8551910	Reedy Point	DE	1973	Today	None	
8555889	Brandywine Shoal Light	DE	1997	Today	Jan 1997-Oct 1997, Mar 1998-Jul 2002, Oct 2012-Nov 2014, Jun 2016-Jun 2017	
8557380	Lewes	DE	1919	Today	None	
8570283	Ocean City Inlet	MD	1997	Today	Jan 1997-Dec 1997 Feb 1999-Aug 2002	
8571421	Bishops Head	MD	2005	Today		
8571892	Cambridge	MD	1979	Today	Jan 1997-May 1997	
8573364	Tolchester Beach	MD	1971	Today	None	
8573927	Chesapeake City	MD	2003	Today		
8574680	Baltimore	MD	1902	Today	None	
8575512	Annapolis	MD	1928	Today	May 2000-Aug 2000	
8577330	Solomons Island	MD	1979	Today	Oct 2013-Apr 2014	
8594900	Washington	DC	1924	Today	Nov 2003-Nov 2004	
8631044	Wachapreague	VA	1978	Today	Jan 2000-Jun 2000, Dec 2001-Mar 2002, Nov 2005-May 2008	
8632200	Kiptopeke	VA	1976	Today	None	
8633607	Dahlgren	VA	2015	Today		
8635750	Lewisetta	VA	1970	Today	None	
8636580	Windmill Point	VA	1996	Today	Aug 2002-Jan 2003	
8637689	Yorktown USCG Training Center	VA	2004	Today		
8638610	Sewells Point	VA	1927	Today	None	
8639901	CBBT, Chesapeake Channel	VA	2017	Today		
8639348	Money Point	VA	1997	Today	Jan 1997-Dec 1997	Not used in Dusek et al. (2022)
8651370	Duck	NC	1978	Today	None	
8652587	Oregon Inlet Marina	NC	1994	Today	None	
8654467	USCG Station Hatteras	NC	2010	Today		
8656483	Beaufort, Duke Marine Lab	NC	1967	Today	None	
8658120	Wilmington	NC	1935	Today	None	
8659163	Wrightsville Beach	NC	2004	Today		
8661070	Springmaid Pier	SC	1976	Today	Jan 2014-Nov 2014	
8665530	Charleston	SC	1921	Today	None	
8670870	Fort Pulaski	GA	1935	Today	None	
8679598	Kings Bay MSF Pier	GA	2022	Today		
8720030	Fernandina Beach	FL	1938	Today	Jan 1997-Feb 1997	
8720218	Mayport (Bar Pilots Dock)	FL	1995	Today	Jan 1997-Dec 2000	
8720219	Dames Point	FL	2013	Today		
8720226	Southbank Riverwalk, St. Johns River	FL	1997	Today	Jan 1997-Apr 1997, Jul 1997-Apr 1998, Nov 1998-Apr 1999, Jul 1999-Sep 2001, Apr 2005-Jun 2006, Oct 2007-Apr 2014	
8720357	I-295 Buckman Bridge	FL	1997	Today	Jan 1997-Apr 1997, Jul 1997-Apr 2003, Jul 2017-Jan 2021	
8721604	Trident Pier, Port Canaveral	FL	1994	Today	None	
8722670	Lake Worth Pier, Atlantic Ocean	FL	2010	Today		
8722956	South Port Everglades	FL	2018	Today		
8723214	Virginia Key	FL	1994	Today	None	
8723970	Vaca Key, Florida Bay	FL	1975	Today	None	
8724580	Key West	FL	1913	Today	None	
8725110	Naples	FL	1965	Jan 2024	Sept 2022-Dec 2022	Used in Dusek et al. (2022), cannot be used as missing data for last half of 2022
8725114	Naples Bay, North	FL	2024	Today		
8725520	Fort Myers	FL	1969	Today	May 1997-Nov 1997	
8726384	Port Manatee	FL	1990	Today	Jan 1997-Jan 1999	
8726520	St. Petersburg	FL	1946	Today	None	
8726607	Old Port Tampa	FL	1996	Today	Jan 1997-Jan 1999, Aug 2001-Apr 2002, Mar 2004-Oct 2004	
8726674	East Bay	FL	2019	Today		
8726724	Clearwater Beach	FL	1996	Today	None	
8727520	Cedar Key	FL	1914	Today	None	
8728690	Apalachicola	FL	1976	Today	None	
8729108	Panama City	FL	1973	Today	Nov 1997-Apr 1998	
8729210	Panama City Beach	FL	1993	Today	Jan 2008-Sep 2013	
8729840	Pensacola	FL	1923	Today	Sep 2004-Jan 2005	
8735180	Dauphin Island	AL	1981	Today	Oct 1997-Sep 2001, Aug 2003-Nov 2003	
8735391	Dog River Bridge	AL	2011	Today		
8735523	East Fowl River Bridge	AL	2011	Today		
8736897	Coast Guard Sector Mobile	AL	2007	Today		
8737048	Mobile State Docks	AL	2007	Today		
8737138	Chickasaw Creek	AL	2011	Today		
8738043	West Fowl River Bridge	AL	2011	Today		
8739803	Bayou La Batre Bridge	AL	2011	Today		
8741533	Pascagoula NOAA Lab	MS	2005	Today		
8747437	Bay Waveland Yacht Club	MS	1978	Today	Feb 1997-Nov 2005	
8760721	Pilottown	LA	2011	Today		
8760922	Pilots Station East, S.W. Pass	LA	2004	Today		
8761305	Shell Beach	LA	2008	Today		
8761724	Grand Isle	LA	1980	Today	None	
8761927	New Canal Station	LA	1982	Today	Jan 1997-Nov 2005	
8761955	Carrollton	LA	2009	Today		
8762075	Port Fourchon, Belle Pass	LA	2003	Today		
8762482	West Bank 1, Bayou Gauche	LA	2003	Today		
8764044	Berwick, Atchafalaya River	LA	2003	Today		
8764227	LAWMA, Amerada Pass	LA	2006	Today		
8764314	Eugene Island, North of, Atchafalaya R	LA	2015	Today		
8766072	Freshwater Canal Locks	LA	2005	Today		
8768094	Calcasieu Pass	LA	2002	Today		
8770475	Port Arthur	TX	2012	Today		
8770520	Rainbow Bridge	TX	1996	Today	Jan 1997-Jul 2002, Jan 2003-Oct 2012, Oct 2013-Jun 2015	
8770570	Sabine Pass North	TX	1985	Oct 2020	Oct 2020-Dec 2022	Used in Dusek et al. (2022), cannot be used as no observations for some of 2020, all of 2021 and 20
8770613	Morgans Point, Barbours Cut	TX	1993	Today	Jan 1997 a couple weeks	
8770777	Manchester	TX	1998	Today		
8770808	High Island	TX	2015	Today		
8770822	Texas Point, Sabine Pass	TX	2011	Today		
8770971	Rollover Pass	TX	2015	Today		
8771013	Eagle Point, Galveston Bay	TX	1993	Today	None	
8771341	Galveston Bay Entrance, North Jetty	TX	2001	Today		
8771367	Sabine Offshore Light	TX	2020	Today		
8771450	Galveston Pier 21	TX	1904	Today	None	

No missing data	36
<2 yr missing	19
>= 2 yr missing, used in Dusek	6
>= 2 yr missing, not used in Dusek	8
Data do not cover training period	77
Data do not cover prediction period	3
Total stations	149
Total used for analysis	**61**

124		8771486 Galveston Railroad Bridge	TX	2013 Today				
125		8771972 San Luis Pass	TX	2012 Today				
126		8772471 Freeport Harbor	TX	2016 Today				
127		8772985 Sargent	TX	2012 Today				
128		8773037 Seadrift	TX	2016 Today				
129		8773146 Matagorda	TX	2012 Today				
130		8773259 Port Lavaca	TX	2015 Today				
131		8773701 Port O'Connor	TX	2016 Today				
132		8773767 Matagorda Bay Entrance Channel	TX	2016 Today				
133		8774230 Aransas Wildlife Refuge	TX	2012 Today				
134		8774770 Rockport	TX	1937 Today	Aug 2017-Jun 2018			
135		8775132 La Quinta Channel North	TX	2021 Today				
136		8775222 Viola Turning Basin	TX	2021 Today				
137		8775237 Port Aransas	TX	2002 Today				
138		8775241 Aransas, Aransas Pass	TX	2016 Today				
139		8775283 Enbridge, Ingleside	TX	2002 Today				
140		8775296 USS Lexington, Corpus Christi Bay	TX	2012 Today				
141		8775792 Packery Channel	TX	2012 Today				
142		8775870 Ball Hall Pier, Corpus Christi	TX	1983 Apr 2022	Apr 2022-Dec 2022			
143		8776139 S. Bird Island	TX	2012 Today				
144		8776604 Baffin Bay	TX	2012 Today				
145		8777812 Rincon Del San Jose	TX	2012 Today				
146		8778490 Port Mansfield	TX	2012 Today				
147		8779280 Realitos Peninsula	TX	2012 Today				
148		8779748 South Padre Island CG Station	TX	2015 Today				
149		8779749 SPI Brazos Santiago	TX	2016 Today				
150		8779770 Port Isabel	TX	1944 Today	None			

S3 Table. CORA-derived HTF prediction performance results, at one month lead, for each station included in the analysis.

	A	B	C	D	E	F	G	H
1	Station	Region	Assimilated?	HL agreement (%)[1]	HL bias[1]	HL MAE[1]	CRPS change (%)[2]	rBSS[1]
2	Eastport, ME	NE	Y	77|83|88|91	0.35|0.28|0.17|0.08	0.35|0.28|0.18|0.11	9	-0.27|-0.22|0.05|0.03
3	Bar Harbor, ME	NE	Y	82|90|92|93	0.21|0.1|-0.04|-0.09	0.22|0.13|0.09|0.09	13	-0.16|-0.1|-0.03|-0.25
4	Portland, ME	NE	Y	79|89|92|96	0.23|0.1|-0.02|-0.05	0.25|0.13|0.09|0.05	14	-0.24|-0.08|0.04|-0.07
5	Boston, MA	NE	Y	75|84|92|94	0.33|0.18|0.04|-0.05	0.33|0.2|0.09|0.06	9	-0.26|-0.16|0.07|0
6	Woods Hole, MA	NE	Y	78|83|96|100	0.17|0.2|0.04|0	0.26|0.23|0.04|0	10	-0.07|-0.07|-0.03|-0.01
7	Nantucket Island, MA	NE	Y	82|91|99|100	0.05|0.08|0|0	0.19|0.1|0.01|0	5	-0.05|0.04|0|0
8	Newport, RI	NE	N	75|88|97|100	0.3|0.12|0.02|0	0.31|0.14|0.04|0	5	-0.15|-0.07|-0.03|-0.01
9	Providence, RI	NE	N	70|82|92|99	0.39|0.22|0.09|0.01	0.4|0.24|0.09|0.01	2	-0.29|-0.15|-0.08|0.04
10	New London, CT	NE	Y	71|93|100|100	0.3|0.04|0|0	0.33|0.08|0|0	0	-0.01|0.04|0|0
11	Bridgeport, CT	NE	Y	79|86|96|99	0.2|0.13|0|-0.01	0.24|0.17|0.04|0.01	7	-0.02|0.04|-0.03|0.04
12	Montauk, NY	NE	Y	77|90|99|100	0.2|0.02|-0.01|0	0.25|0.1|0.01|0	2	-0.07|0.01|0|0
13	Kings Point, NY	NE	Y	76|82|86|96	-0.19|-0.14|-0.16|-0.06	0.25|0.18|0.16|0.06	13	0.04|0.03|-0.04|0.17
14	The Battery, NY	MA	Y	85|90|95|100	0.01|0.04|-0.02|0	0.16|0.1|0.05|0	4	0.01|-0.02|0|0
15	Bergen Point West Reach, NY	MA	N	78|83|95|100	0.21|0.17|0.02|0	0.24|0.19|0.05|0	3	-0.12|-0.14|0.02|0.01
16	Sandy Hook, NJ	MA	Y	82|85|94|99	0.15|0.15|0.05|0	0.19|0.17|0.07|0.01	3	-0.06|-0.03|-0.01|0.01
17	Atlantic City, NJ	MA	Y	79|86|97|100	0.21|0.12|0|0	0.22|0.14|0.03|0	1	-0.07|-0.02|0|0.01
18	Cape May, NJ	MA	Y	75|80|95|100	0.26|0.19|0.02|0	0.28|0.21|0.05|0	2	-0.1|-0.05|0|0.01
19	Philadelphia, PA	MA	N	67|77|97|100	0.29|0.24|0.01|0	0.37|0.28|0.03|0	-6	0.02|0.08|-0.01|0
20	Reedy point, DE	MA	Y	76|76|95|100	0.07|0.26|0.05|0	0.25|0.27|0.05|0	7	-0.03|0.02|-0.14|-0.03
21	Lewes, DE	MA	Y	78|82|95|100	0.21|0.17|0.02|0	0.23|0.19|0.05|0	1	-0.06|-0.03|0.02|0.01
22	Cambridge, MD	MA	N	72|85|100|100	0.29|0.09|0|0	0.3|0.15|0|0	-5	-0.1|-0.01|0|0
23	Tolchester Beach, MD	MA	N	88|85|100|100	0.01|-0.14|0|0	0.13|0.15|0|0	1	0|-0.01|0.01|0
24	Baltimore, MD	MA	Y	86|89|100|100	0.08|-0.04|0|0	0.14|0.11|0|0	-2	-0.01|0|0.01|0
25	Annapolis, MD	MA	N	90|86|100|100	-0.04|-0.14|0|0	0.1|0.15|0|0	0	0.01|0|-0.01|0
26	Solomons Island, MD	MA	N	91|83|100|100	0.06|0.16|0|0	0.09|0.17|0|0	-1	-0.05|-0.04|0|0
27	Washington, DC	MA	N	62|71|100|100	0.39|0.12|0|0	0.48|0.3|0|0	1	-0.1|0|0.04|0
28	Wachapreague, VA	MA	N	67|76|95|100	0.28|0.24|0.04|0	0.34|0.26|0.05|0	15	-0.07|-0.01|0|0
29	Kiptopeke, VA	MA	N	52|71|97|100	0.52|0.31|0.03|0	0.52|0.31|0.03|0	5	-0.15|-0.09|0.01|0.01
30	Lewisetta, VA	MA	Y	94|89|98|100	0|-0.02|0|0	0.06|0.11|0.02|0	0	0|0|0|0
31	Windmill Point, VA	MA	N	91|85|99|100	-0.06|-0.09|-0.01|0	0.09|0.15|0.01|0	0	0.02|0|-0.01|0
32	Sewells Point, VA	MA	N	85|83|97|100	0.06|0.13|0.02|0	0.15|0.17|0.03|0	2	-0.03|-0.04|-0.01|0.01
33	Money Point, VA	MA	N	83|84|97|100	0.08|0.11|0.01|0	0.17|0.16|0.03|0	2	-0.05|-0.05|-0.01|0
34	Duck, NC	MA	Y	84|90|97|100	0.12|0.08|0|0	0.17|0.1|0.03|0	2	-0.06|-0.02|-0.01|-0.01
35	Oregon Inlet Marina, NC	MA	N	53|78|100|100	-0.19|-0.27|0|0	0.6|0.27|0|0	5	0.01|0.06|-0.02|0
36	Beaufort, Duke Marine Lab, NC	SE	Y	86|90|98|100	0.01|-0.07|-0.02|0	0.14|0.1|0.02|0	7	-0.02|-0.1|-0.07|0
37	Wilmington, NC	SE	N	69|80|99|100	0.01|0.08|0|0	0.34|0.23|0.01|0	32	0.06|0.04|0|0
38	Springmaid Pier, SC	SE	Y	85|92|96|99	0.14|0.02|-0.03|-0.01	0.16|0.08|0.04|0.01	-3	0|-0.01|-0.07|-0.04
39	Charleston, SC	SE	Y	78|84|91|99	0.11|0.14|0.09|0.01	0.23|0.16|0.09|0.01	6	0|0.03|0.09|0.07
40	Fort Pulaski, GA	SE	Y	77|83|92|98	0.12|0.13|0.06|0	0.24|0.18|0.08|0.02	-1	0.02|0.03|0.01|-0.03
41	Fernandina Beach, FL	SE	Y	84|90|97|99	0.03|-0.01|-0.01|-0.01	0.16|0.11|0.03|0.01	4	-0.01|-0.01|-0.07|-0.13
42	Mayport (Bar Pilots Dock), FL	SE	Y	81|90|98|100	0.14|0.04|-0.01|0	0.19|0.1|0.03|0	6	0.01|-0.02|-0.02|-0.01
43	Trident Pier, Port Canaveral, FL	SE	Y	85|92|96|100	0.1|0.05|0.01|0	0.15|0.08|0.04|0	1	-0.01|-0.01|0.02|-0.01
44	Virginia Key, FL	SE	Y	75|88|99|100	-0.04|0.07|0|0	0.26|0.12|0.01|0	4	-0.05|0.01|-0.02|0
45	Vaca Key, Florida Bay, FL	SE	Y	76|87|100|100	0.22|0.11|0|0	0.26|0.14|0|0	16	0.02|0.02|0.02|0
46	Key West, FL	SE	Y	89|95|100|100	0.05|0.03|0|0	0.12|0.05|0|0	3	0|0.03|0|0
47	Fort Myers, FL	EG	N	64|83|100|100	-0.08|0.02|0|0	0.4|0.19|0|0	0	-0.05|0|-0.01|0
48	St. Petersburg, FL	EG	Y	86|93|100|100	-0.02|-0.03|0|0	0.15|0.07|0|0	7	-0.03|-0.03|0.01|0
49	Clearwater Beach, FL	EG	N	78|80|99|100	-0.15|-0.23|-0.02|0	0.24|0.23|0.02|0	16	-0.09|-0.08|-0.01|0
50	Cedar Key, FL	EG	Y	78|79|97|100	0.02|0.13|0.03|0	0.22|0.23|0.04|0	-1	0.05|0.07|0.02|0.01
51	Apalachicola, FL	EG	N	72|89|100|100	-0.19|-0.09|0|0	0.31|0.12|0|0	31	-0.12|0.01|0|0
52	Panama City, FL	EG	N	78|86|100|100	0.04|-0.1|0|0	0.22|0.16|0|0	14	-0.06|-0.06|0|0
53	Panama City Beach, FL	EG	Y	80|88|99|100	0.08|-0.03|0|0	0.21|0.13|0.01|0	6	-0.07|-0.06|-0.02|0
54	Pensacola, FL	EG	Y	79|85|99|100	0.19|0.14|0.01|0	0.22|0.16|0.01|0	0	0.01|-0.04|-0.01|0
55	Dauphin Island, AL	EG	Y	83|90|99|100	0.09|0|-0.01|0	0.18|0.1|0.01|0	4	0|-0.02|-0.02|0
56	Bay Waveland Yacht Club, MS	EG	Y	73|69|90|100	0.23|0.32|0.11|0	0.28|0.33|0.11|0	0	-0.05|-0.12|-0.08|0.01
57	Grand Isle, LA[3]	EG	Y	27|33|84|100	1.53|1.34|0.27|0	1.53|1.34|0.27|0	86	-1.64|-3.56|-1.65|-0.04
58	Morgans Point, Barbours Cut, TX	WG	N	66|60|85|100	0.37|0.43|0.15|0	0.39|0.45|0.15|0	-7	-0.14|-0.21|-0.07|0
59	Eagle Point, Gaveston Bay, TX	WG	N	64|33|67|99	-0.45|-0.89|-0.37|-0.01	0.45|0.89|0.37|0.01	18	0.05|0.01|0.02|0.01
60	Galveston Pier 21, TX	WG	N	76|68|88|100	-0.24|-0.33|-0.12|0	0.24|0.33|0.12|0	5	-0.02|-0.01|0.06|-0.01
61	Rockport, TX[3]	WG	Y	51|42|80|100	0.85|0.86|0.26|0	0.85|0.86|0.26|0	40	-0.56|-1.04|-0.8|-0.01
62	Port Isabel, TX	WG	Y	77|86|97|100	0.06|-0.03|-0.03|0	0.25|0.14|0.03|0	3	-0.03|-0.01|0.01|0
63								
64	[1]Values are presented for the four considered flood thresholds in increasing order: MHHW + 0.15 m | MHHW+ 0.30 m | MHHW + 0.45 m | MHHW + 0.60 m							
65	[2]Positive (negative) values indicate weaker (stronger) HTF model performance when using CORA as input relative to using gauge observations as input							
66	[3]Grand Isle, LA and Rockport TX are not included in the average values presented in the main text. More details on these stations are given in S4 Appendix.							

S4. Appendix. Explanation of CORA errors at Grand Isle, L.A. and Rockport, T.X.

Agreement between CORA-derived and gauge-derived HTF predictions was found to be particularly weak at Grand Isle, L.A. and Rockport, T.X. Further analysis revealed systemic errors in CORA water levels and derived tide predictions at these locations, as will be described further in this appendix and shown in Figures S4-1 and S4-2.

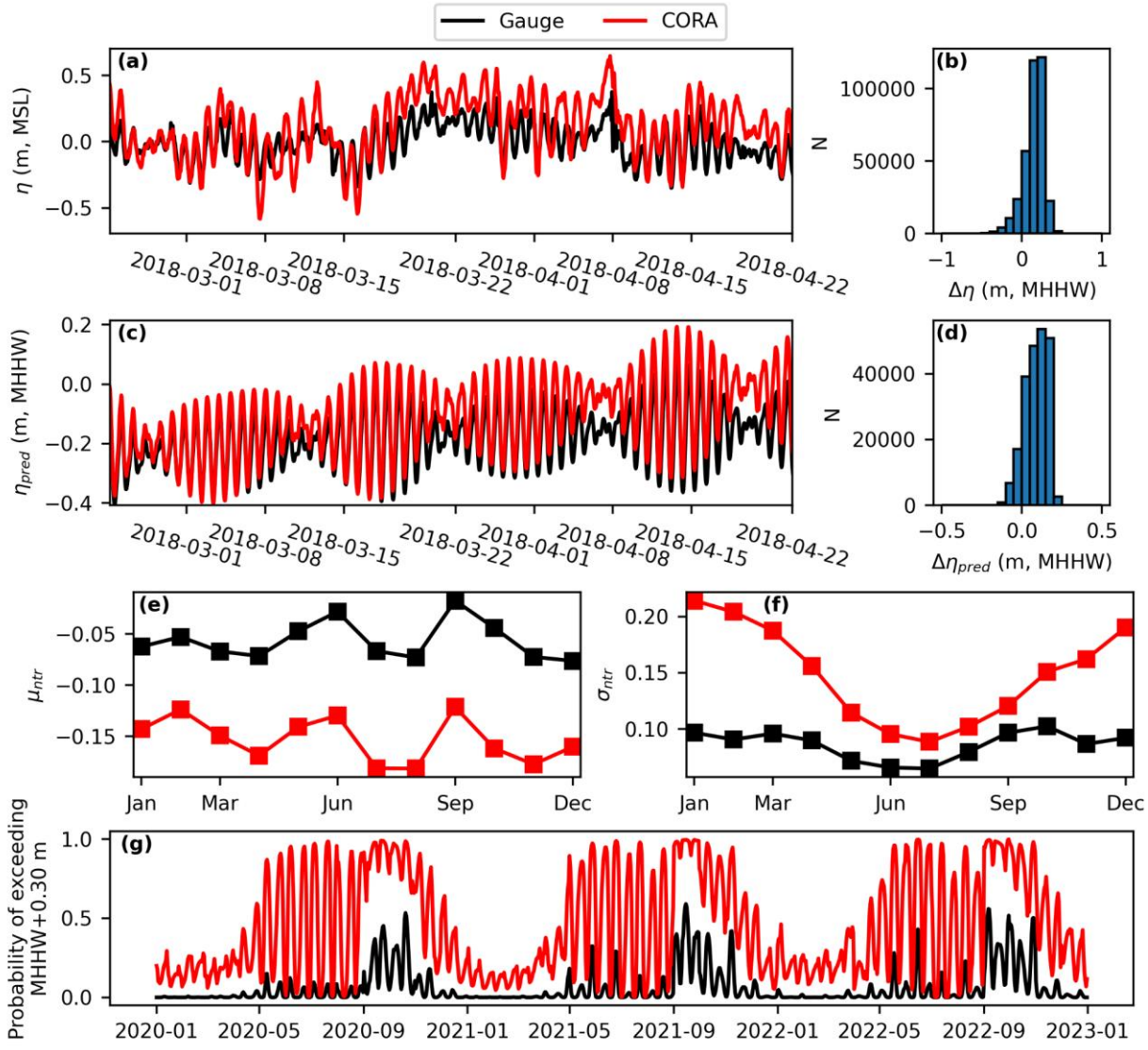

Figure S4-1. Explanation of differences between CORA-derived and gauge-derived HTF model performance at Grand Isle, L.A. (a) Observed hourly water levels during an example period. (b) Distribution of hourly errors in CORA water levels for the full training period, 1997 through 2021. (c) Hourly tide predictions during an example period. (d) Distribution of hourly errors in CORA tide predictions for the full training period, 1997 through 2022. (e) Monthly mean non-tidal residual. (f) Standard deviation

around the monthly mean non-tidal residual. (g) The resulting daily probability of high tide flooding above $MHHW + 0.30$ m.

At Grand Isle, CORA water levels exhibit a larger range than observed water levels. At times, CORA low waters are lower than observations, other times higher, while high waters are frequently overestimated (Figure S4-1a). When transferred to the derived MHHW datum, which is within 2 cm of the observed value, CORA water levels are biased high by 13 cm on average and the distribution of differences is left skewed (Figure S4-1b). The differences in water levels result in CORA-derived tide predictions with over-estimated tide range and a high bias, by 9 cm on average though particularly for high tides, and a left-skewed distribution of differences relative to gauge-derived tide predictions (Figure S4-1c,d). The combination of these errors leads to low-biased μ_{NTR} for CORA by ~10 cm (Figure S4-1e) and CORA-derived σ_{NTR} which is biased high relative to the gauge by as much as 100% during January and December (Figure S4-1f). While the high-biased tide predictions and low-biased μ_{NTR} largely offset each other in the HTF probability computation, the larger σ_{NTR} increases CORA-derived HTF probability at all times relative to the gauge (Figure S4-1g).

At Rockport, a systemic high bias of 11 cm on average is observed in CORA water levels on MSL (Figure S4-2a). Yet, the computed MHHW value for CORA is <1 cm different from the published value at the gauge. Therefore, the high bias remains when CORA water levels are transferred to MHHW (Figure S4-2b) and propagates to the derived tide predictions, which are biased high by 17 cm on average while tidal range is underestimated (Figure S4-2c,d). While σ_{NTR} are similar in this case (Figure S4-2f), these differences lead to CORA-derived μ_{NTR} that is biased low by 7 cm (Figure S4-2e). The high bias in the tide predictions, which is larger than the low bias in μ_{NTR}, increases CORA-derived HTF probability at all times relative to the gauge (Figure S4-2g). Note that this is a similar end-result to Grand Isle though arises through a different mechanism.

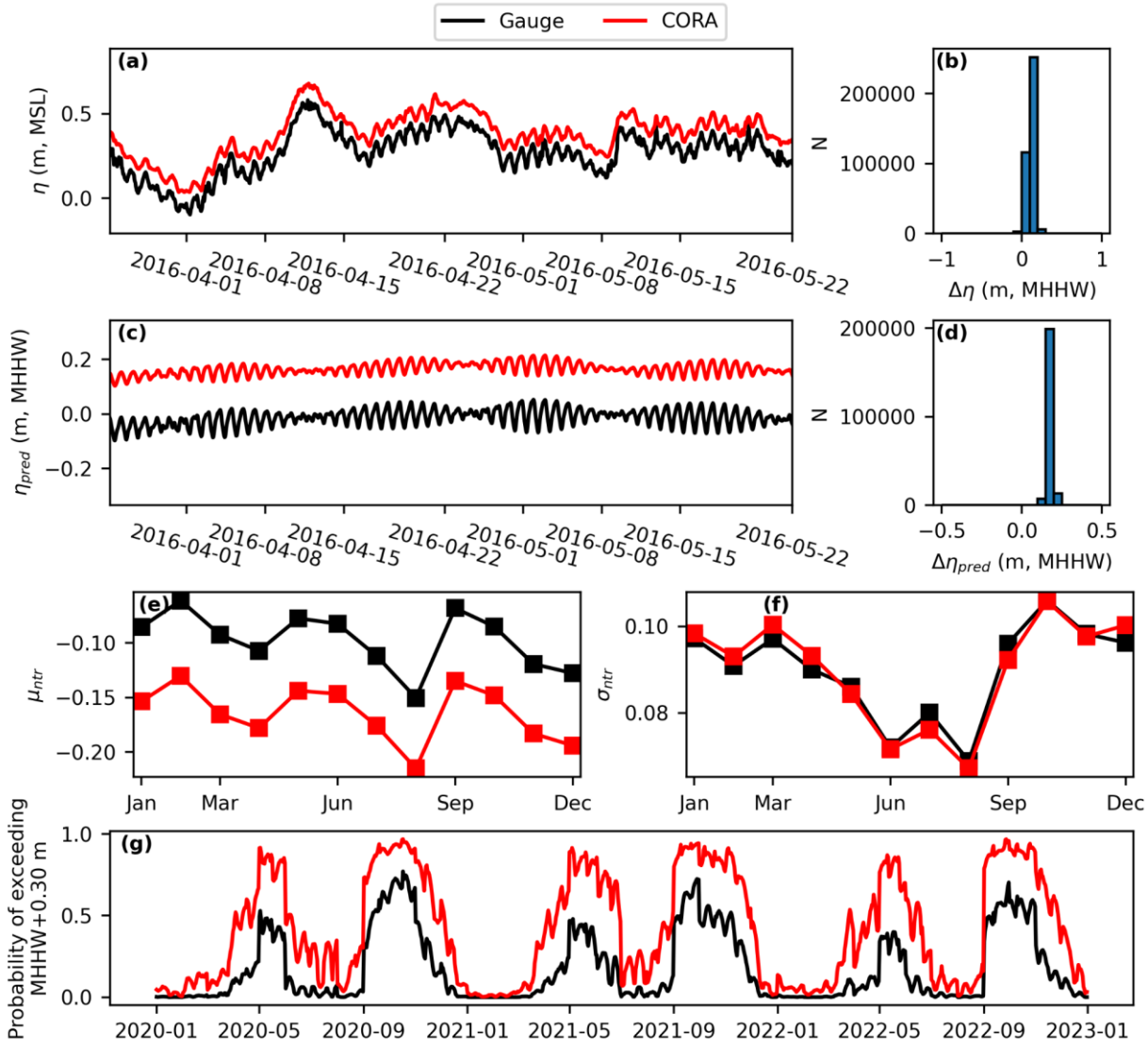

Figure S4-2. Explanation of differences between CORA-derived and gauge-derived HTF model performance at Rockport, T.X. (a) Observed hourly water levels during an example period. (b) Distribution of hourly errors in CORA water levels for the full training period, 1997 through 2021. (c) Hourly tide predictions during an example period. (d) Distribution of hourly errors in CORA tide predictions for the full training period, 1997 through 2022. (e) Monthly mean non-tidal residual. (f) Standard deviation around the monthly mean non-tidal residual. (g) The resulting daily probability of high tide flooding above $MHHW + 0.30$ m.